Introduction

CHAPTER - 1

1.1 Solar Energy

The world now uses energy at the rate of approximately 4.1 × 1020 joules/yr, equivalent to a continuous power consumption of 13 trillion watts, or 13 terawatts (TW). Even with aggressive conservation and energy efficiency measures, an increase of the Earth's population to 9 billion people, accompanied by rapid technology development and economic growth world-wide, is projected to produce more than double the demand for energy (to 30 TW) by 2050, and more than triple the demand (to 46 TW) by the end of the century. The world's sources of fossil fuels are drying up faster than the earth can renew them. Fossil fuels, like coal and oil take the earth thousands of years to reproduce and their continued use produces harmful side effects such as pollution that threatens human health and greenhouse gases associated with climate change that what we call today the global warming It is the matter of great concern for all. So, an effective alternative source of energy must be explored that fulfill our demands as well as it would be clean and renewable. The two prominent options to meet this demand are nuclear power and solar power. Nuclear power is conceptually viable option as the resource producing nuclear energy i.e. uranium is limited as well as the waste products are hazardous too. Therefore, solar power is a promising source of future energy supplies because not only is it clean, it's remarkably abundant**.** Solar energy is radiant energy that is produced by the sun. The sun deposits 120,000 TW of radiation on the surface of the Earth, far exceeding human needs even in the most aggressive energy demand scenarios. So, it is clear that solar energy can be exploited on the needed scale to meet global energy demand in a carbon-neutral fashion without significantly affecting the solar resource. Solar power can be utilized in TWO different ways –

a) Solar Electricity

b) Solar Thermal

Our focus is on solar electricity for which we have to employ new ideas to generate electricity using solar cell technology.

1.2 Solar cell

Solar power can be converted directly into electrical power in photovoltaic (PV) cells, commonly called solar cells. The solar power is converted into electric power through photovoltaic effect.

1.2.1 Photovoltaic Effect

The photovoltaic effect was first observed by A.E Becquerel in 1839. However, the birth of the modern era of PV solar cells occurred in 1954, when D. Chapin, C.Fuller, and G. Pearson at Bell Labs demonstrated solar cells based on p-n junctions in single-crystal Si with efficiencies of 5–6%. This original Si solar cell still works today — single-crystal Si solar cells dominate the commercial PV market.

The **photovoltaic effect** is the creation of voltage or electric current in a material upon exposure to light. The photovoltaic effect differs from photoelectric effect in that electrons are transferred between different bands (i.e., from the valence to conduction band) within the material, resultingin the buildup of voltage between two electrodes.

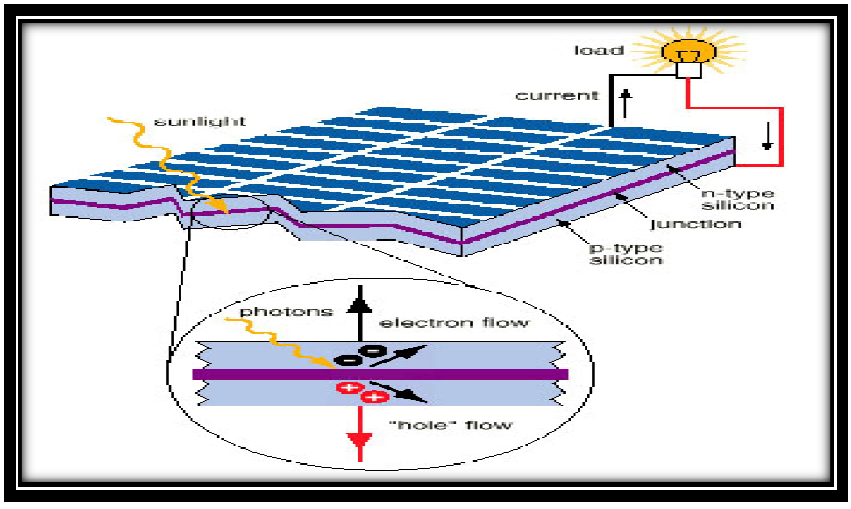

Fig.1.1 Photovoltaic Effect in Solar Cell

The photovoltaic effect used in solar cells allows direct conversion of light energy from Sun's rays into electricity, by way of the generation, and transport inside a semiconductor material, of positive and negative electric charges ,through the action of light.

Photovoltaic cells generally consist of a light absorber that will only absorb solar photons above certain minimum photon energy. This minimum threshold energy is called the "energy gap" or "band gap" (Eg); photons with energies below the band gap pass through the absorber, while photons with energies above the band gap are absorbed. The light absorber in PV cells can be either inorganic semiconductors, organic molecular structures, or a combination of both.

1.2.2 Photovoltaic Market

According to a Solar buzz report[c], global PV market installations reached a record high of 6.43 gigawatt in 2009 (Fig. 1.2), representing a growth of 6% over the previous year. The top three European countries are Germany, Italy, and Czech Republic. The PV industry generated US$ 38 billion in global in 2009, while successfully raising over US$13.5 billion in equity and debt up 8% on 2008. In 2010 and also over the next 5 years, the PV industry is expected to return to high growth, and the global market will be 2.5 times its current size by 2014, and the annual industry revenues will approach US$ 100 billion then.

c http://www.solarbuzz.com/marketbuzz2010-intro.htm

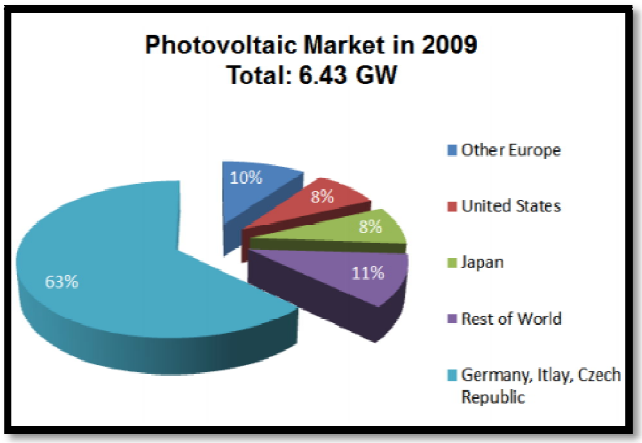

Figure 1.2. Photovoltaic market in 2009 (Data taken from Solar buzz *http://www.solarbuzz.com/marketbuzz2010-intro.htm*)

1.2.3 Solar Cell Generation

Photovoltaic (PV) energy conversion is attracting more and more attention as the need for renewable energy sources replacing current environmental critical technologies becomes more urgent. PV is an attractive way of producing electrical energy directly from sunlight, without producing noise, toxic substances and greenhouse gas emission, while requiring very little maintenance.

1.2.3.1 Semiconductor-based Conventional Solar Cells

Bulk semiconductors absorb optical photons to generate unbound e-h pairs. Bandgap (E_g) of the semiconductor material plays an important role in the process of photo-generation. In an ideal case, photons with an energy $h_v < E_g$ will not contribute to the photo-generation, whereas all photons with an energy $h_v > E_g$ will each contribute to the photo-generated electron-hole pair followed by spontaneous recombination. If these electron-hole pairs can be separated before they spontaneously recombine, a current can be generated. However, several energy-loss mechanisms limit the current extraction from such a device. When an electron is excited to a level above the edge of the conduction band, the energy in excess of the band gap will be lost as heat as a result of e- phonon coupling, and the electron is relaxed to the edge of the conduction band. Finally, the electron at the band edge will spontaneously recombine with a hole, radiatively or non-radiatively. Schematic diagram in Fig. 1.3 shows a semiconductor based traditional p-n junction solar cell.

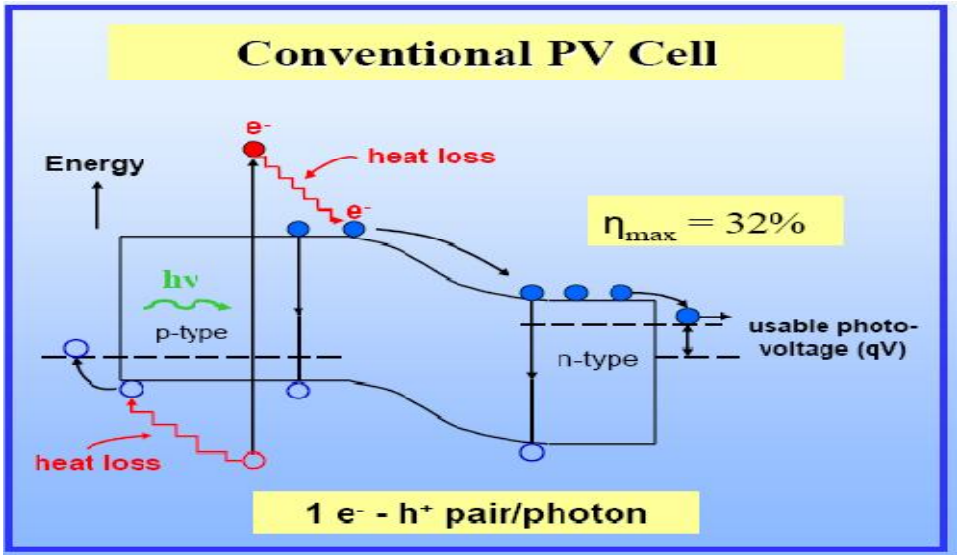

Fig. 1.3: Schematic diagram of a semiconductor based traditional p-n junction solar cell (Fig taken from J. Nozik, NREL report)

As a result of above-discussed energy loss mechanisms, and considering the fact that one photon generates only one e-h pair, the maximum achievable efficiency of a solar device has been computed to be 33%.Traditional single junction silicon solar cells today exhibit efficiencies between 11-20% as a result of light loss due to reflection from the front surface of the cell, shadowing by the electrical contacts, and ohmic losses at the semiconductor/electrode junctions.

Currently the photovoltaic market is dominated by Crystalline Si based solar cell having power conversion efficiency 25% [1]. Commercialized product has typical efficiency of about 15-18%. Due to fragile nature of silicon wafer, the fabrication process is complex and it is more expensive resulting in high cost. To reduce the manufacturing problem and cost reduction of first generation, second generation solar cells was developed which are much cheaper to produce than first generation solar cell but the PCEs remain lower than for the first generation solar cells, and the promise of low cost power has not been realized yet.

Third generation solar cell are developed to come out with these problems of first and second generation. They are promising candidate for low cost fabrication but efficiency enhancement is the main issue in this generation. From the last decade, Researchers are continuously trying to construct photovoltaic devices which are based on the mixture of inorganic nanoparticles and conjugated polymers. The aim of this inorganic-organic hybrid material is to maintain the

flexibility with polymer and high charge mobility from the nanoparticles or we can use, blue absorbance from polymer and red absorbance from the nanoparticles. The efforts in this direction are made by the scientist and researchers due to a serious problem of global temperatures in front of all over the world.

Global temperatures will increase by 1 to 6 °C and CO_2 concentration will exceed the range of 560 to 970 parts per million during the 21st century [2]. This creates the awareness and increasing need for renewable energy resources. Approximately the 80% of world energy supply comes from the fossil fuels [3]. Unfortunately photovoltaic (PV) energy only contributes 0.04% of the total energy production [4] whereas the earth receives enough energy in an hour to fulfill the yearly demand. The main reason for low utilization photovoltaic devices in energy market is its higher cost. The inorganic organic hybrid approach is useful to resolve this problem due to its low fabrication cost and flexibility.

Currently the photovoltaic industry is dominated by silicon based photovoltaic. Single and multi-junction thin film PV is also contributes the PV market because of its ability of high power conversion efficiency (PCE). The PCE of hybrid solar cell is low near about 3% [5], but they are strong candidate of PV market due to Light weight, Low production cost and high optical absorption [6, 7] like pure organic solar cell based on small molecules and carbon nanotubes. Despite substantial progress in solar cell architecture, design and rational choice of the donor-acceptor materials over the past two decades, organic PVs are still unable to overcome the 6–7% barrier of conversion efficiency [8, 9]. In terms of the low conversion efficiency, there are currently at least four major fundamental aspects making organic PVs for commercial applications as compared with conventional semiconducting solar cells: (i) low carrier mobility, (ii) lack of absorption in the red/NIR part of spectrum, (iii) poor environmental stability, and (iv) excitonic character of photocarrier generation. The source of photocarriers in organics is small radius excitons generated as a result of photon absorption. Excitons in organics have a binding energy in the range 200–400 meV [10, 11], which is considerably higher than the binding exciton energy for semiconductor materials ~ 2–40 meV [12]. Thermal energy at room temperature is not sufficient (~25 meV) for exciton dissociation to hole and electron in the bulk medium. Therefore, exciton dissociation should occur at the interface between the donor and acceptor materials with proper HOMO and LUMO energy levels. The mechanism of exciton dissociation is not

completely understood, however the major factor governing the charge separation at the interface is the charge transfer process between the donor and acceptor components. After charge separation, holes and electrons move to the opposite electrodes owing to drift (induced by the electric field at the interface) and diffusion (gradient of the charge concentration from the interface to the surface). In the case of a flat heterojunction, the diffusion length of the singlet excitons (several tens nanometers) should be comparable with the thickness of at least of one active layer (donor or acceptor) to minimize energy loss, otherwise not all excitons are able to reach the interface. However, at such small thickness, the absorbed energy is very low since the penetration length of incident light for organics is typically more than 100 nm. The possible solution could be formation of bulk heterojunctions (blend of donor and acceptor materials) with separation scale factor comparable with the excitonic diffusion lengths and relatively thick films to absorb more light energy. Nevertheless, an increase of the film thickness should result in a longer photocarrier pathway to the external electrodes, which reduces the conversion efficiency owing to carriers trapping and lower carrier mobility. An alternative to pure organic PVs is the class of organic-inorganic hybrid solar cells [13-17], where heterojunction is formed between inorganic semiconductors and organic compounds (small molecules, oligomers, polymers, carbon nanotubes). An advantage of hybrid PVs over organics PVs lies in the high carrier mobility of the semiconductor and the light absorption at longer wavelengths than for organic compounds. On the other hand, the existence of the organic component allows hybrid solar cells to be superior over conventional semiconducting PVs in terms of cost efficiency, scalable wet processing, the variety of organic materials (mismatch between inorganic components can be minimized or prevented), light weight, and flexibility. Moreover, the recent progress in advanced semiconducting nanostructures in combination with organic nanomaterials [e.g., fullerenes and carbon nanotubes (CNTs)] opens new opportunities to overcome the 10% barrier of conversion efficiency for hybrid solar cells in the near future. The band engineering can be a useful instrument in the design of the hybrid solar cell architecture; however it is not as straightforward as for semiconducting PVs. Thus, the PV performance of hybrid solar cell can be readily optimized by tuning the band structure of organic component (work function, band gap, Fermi level) for the best matching with the corresponding band structure of the inorganic counterpart**.**Figure.1.4 shows the classification of hybrid solar cell based on different organic-inorganic component.

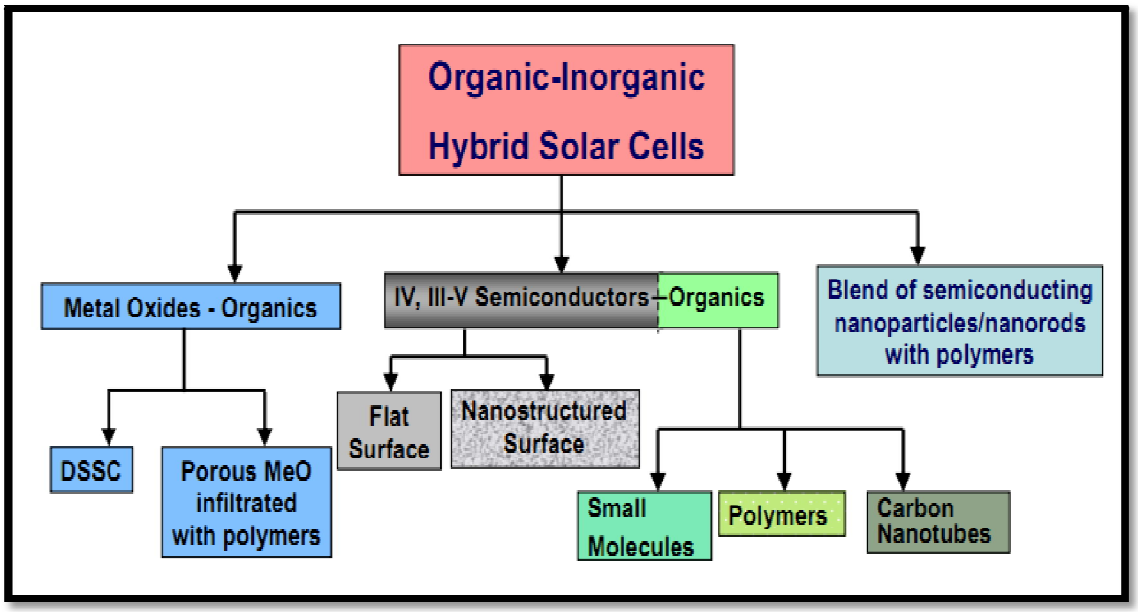

Figure 1.4. Classification of Hybrid solar cell (Image is copied from reference no. 18) www.mdpi.com/journal/energies

1. 2.3.2 Semiconductor NC's based Hybrid Solar Cell

ZnO NCs have also attracted attention for being used in hybrid solar cells because of less toxicity than II-VI semiconductors and are relatively easy to synthesize in large quantities. Devices based on blends of MDMO-PPV and ZnO NCs at an optimized NC content (67wt %) presented the best PCE of 1.4% [19]. By using P3HT as donor polymer which has a higher hole mobility, the efficiency was optimized up to 2% with a composite film containing 50 wt% ZnO NCs [20]. Zinc oxide is a large band gap material, due to this its absorption of light is low and another disadvantage is the low solubility of ZnO NC's in solvents which are commonly used for dissolving conjugated polymers [21]. Low solubility of ZnO NC's hindered the interaction with polymer and affects the efficiency of the devices.

Low band gap NCs such as CdTe, PbS, and PbSe NCs are promising acceptor materials due to their ability of absorbing light at longer wavelengths which may allow an additional fraction of the incident solar spectrum to be absorbed. For instance, CdTe NCs have a smaller band gap compared to CdSe NCs, while their synthesis routes including shape control are similar to CdSe NCs [22].

Further lowering of the NC band gap could be achieved by using semiconductors such as PbS or PbSe. Zhang et al. have reported hybrid solar cells based on blends of MEH-PPV and PbS NCs, but unfortunately the PCEs were very low (0.001%)[23]. Watt et al. have developed a novel surfactant-free synthetic route where PbS NCs were synthesized in situ within a MEH-PPV film [24, 25]. In general, using low band gap NCs as electron acceptor in polymer/NCs system has been not successful yet, because energy transfer from polymer to low band gap NCs is the most likely outcome, resulting in inefficient exciton dissociation. Recently it has been demonstrated that Si NCs are promising acceptor material for hybrid solar cells due to the abundance of Si compounds, non-toxicity, and strong UV absorption. Hybrid solar cells based on blends of Si NCs and P3HT with a PCE above 1% have been reported [26]. Si NCs were synthesized by radio frequency plasma via dissociation of silane, and the size can be tuned between 2 and 20 nm by changing chamber pressure, precursor flow rate, and radio frequency power. Devices made out of 35 wt% Si NCs, 3-5 nm in size, exhibited a PCE of 1.15% under AM1.5 G illumination which is a promising first result.

NCs	Polymer	d(nm)	Aspect ratio	NC wt%	Cathode	P(mW/cm2)	Voc(V)	Jsc(mA/cm^2)	FF	PCE(%)	Ref
CdS	MEH-PPV	4	10	86	Al	100	0.85	2.96	0.47	1.17	180
CdTe	MEH-PPV	3.4	5	90	LiF/Al	100	0.37	0.49	0.27	0.05	174
PbS	MEH-PPV	4	1	50-60	Al	5	1	0.13	0.28	0.7	181
PbSe	P3HT	6	1	80	Al	100	0.35	1.08	0.37	0.14	182
Si	P3HT	3-5	1	50	Al	100	0.8	3.8	0.47	1.47	183
Si	P3HT	3-5	1	35	Al	100	0.75	3.3	0.46	1.15	179
SnO2	MDMO-PPV				Au	100	0.63	0.32	0.42	0.085	184
TiO2	P3HT	4-5	5-10	50	Al	100	0.69	2.62	0.63	1.14	185
TiO2	P3HT	20-40	1	60	Al	100	0.44	2.76	0.4	0.42	186
ZnO	P3HT			50	Al	100	0.75	5.2	0.52	2.0	169
ZnO	MDMO-PPV	5	1	67	Al	71	0.81	2.4	0.59	1.6	171
ZnO	P3HT			15[a]	LiF/Sm/Al	100	0.83	3.5	0.50	1.4	187
ZnO	MDMO-PPV			15[a]	Al	90	1.14	2.0	0.42	1.1	188
ZnO	P3HT		1	65	Al	100	0.69	2.38	0.55	0.9	172
ZnO	APFO-3			67	Al	100	0.51	3.1	0.36	0.45	189

Table 1.1. Selected performance parameters of hybrid solar cells based on NCs and conjugated polymer (Copied from reference 27).

1.3. Semiconductor Nanocrystals (Quantum Dots)

In a bulk semiconductor material, the energy levels are closely spaced within bands. The number of available energy levels given in an interval of energy is described as the density of state. In the case of a bulk semiconductor the top occupied band, known as the valence band, is mostly filled. The conduction band of a semiconductor is mostly empty, and it is separated from the valance band by a bad gap where the density of states within the gap for a pure semiconductor is zero. Electrons in the valence band are not free electrons because they are bonded by Coulomb forces formed by the nucleus and the covalent bonds formed by the neighboring electrons. If an electron in the valence band gains energy that is greater than or equal to band gap energy, the electron can breaks these bonds to dissociate from the atom and become associated with the conduction band, yet subjected to the periodic potentials of the lattice. This process therefore, forms an electron and a hole in the conduction and valance bands, respectively. This vacancy can be filled easily by another electron in the valence band. In other words, the vacancy can move freely in the layers due to continuous density of state in the bulk material. Since this generated electron and hole pair can move freely in the lattice of the bulk semiconductor, the pairs are unbounded. When a semiconductor having bulk properties is reduced in size to a few hundred atoms (zero dimension), the density of states in valence and conduction band is changed drastically. The continuous density of state in the bands is replaced by a set of discrete energy levels, i.e S, P and D levels, which may have energy level spacing, e.g. Ep –Es, much larger than the thermal energy k_BT (at room temperature).[28] This new arrangement of density of states in quantum levels changes the optical and electronic properties of the material. In semiconductor quantum dots, excitation of an electron by optical radiation into the unfilled conduction band to create an electron-hole pair requires more energy that that required by a bulk semiconductor of the same material.[28] In quantum dot, the electron-hole pairs generated by absorption of photons are not free as in bulk material because of the discrete nature of the energy levels. These bound electron-hole pairs are known as excitons. Also, when the electron and hole are confined within a particle dimension that is closer to or less than the Bohr exciton size, they interact strongly with one another through Coulomb forces. As the size of a semiconductor nanocrystal decreases below the bulk semiconductor Bohr exciton size, the

exciton experiences increasingly strong confinement effects which significantly alter the allowed energy levels and result in increasingly discrete electronic structures.[28]

In theory, the separation of energy levels is mainly governed by the dimensionality of the semiconductor dot. As explained in the above section, when the size of the material is reduced from bulk to nano, the density of state is changed from being continuous to discrete by replacing continuous energy band with discrete energy levels. Then these discrete levels can be found by solving the Schrodinger equation for different particle dimensions. In the case of a bulk semiconductor material, electron wave function is delocalized and allows electrons to move freely throughout the entire medium. Then, one can use free particle wavefunction without any confinement condition to solve the Schrodinger equation for finding possible energy values. According to this analysis the energy of the electron in three-dimensional (3D) free space can be expressed as

$$E(k)=\hbar^2(k_x^2+k_y^2+k_z^2)/2m_e^* \qquad (1)$$

where k is a wave vector and m_e^* is the effective mass of an electron. As the dimensions of the semiconductor is reduced, the energy of the discrete states for 2D (thin films), 1D (nano wires) and 0D (quantum dots) for spatial dimensions of Lx, Ly, and Lz can be given by,

For 2D $E(k)= \hbar^2 n_x^2/8m_e^* L_x^2 + \hbar^2(k_y^2+k_z^2)/2m_e^*$ (2)

For 1D $E(k)= \hbar^2 (n_x^2/8m_e^* L_x^2 + n_y^2/8m_e^* L_y^2)+\hbar^2 k_z^2/2m_e^*$ (3)

And for 0D $E(k)= \hbar^2 (n_x^2/8m_e^* L_x^2 + n_y^2/8m_e^* L_y^2 + n_z^2/8m_e^* L_z^2)$ (4)

Where, $k_x=\pi(n_x^2/L_x^2)^{1/2}$, $k_y=\pi(n_y^2/L_y^2)^{1/2}$ and $k_z=\pi(n_z^2/L_z^2)^{1/2}$for a bound quantum dot. Similarly, the energy eigen values for spherical quantum dots are given by,[29]

$$E^h = \frac{\hbar^2}{2m_h}\left(\frac{\alpha_{n_h \ell_h}}{R}\right)^2 \qquad (5)$$

$$E^e = E_g + \frac{\hbar^2}{2m_e}\left(\frac{\alpha_{n_e \ell_e}}{R}\right)^2 \quad (6)$$

$$E = E^h + E^e = E_g + \frac{\hbar^2}{2m_e}\left(\frac{\alpha_{n_e \ell_e}}{R}\right)^2 + \frac{\hbar^2}{2m_h}\left(\frac{\alpha_{n_h \ell_h}}{R}\right)^2 \quad (7)$$

In these equations $\alpha_{n_e \ell_e}$ is the n^{th} root of the ℓ^{th} order Bessel function for the electron while $\alpha_{n_h \ell_h}$ is the n^{th} root of the ℓ^{th} order Bessel function for the hole.

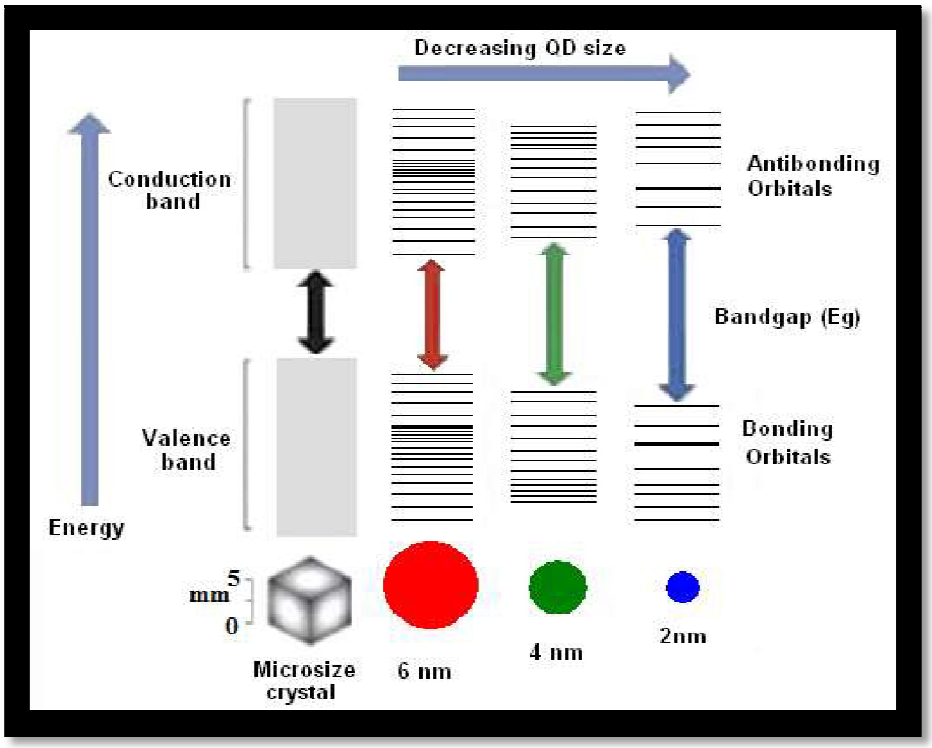

Fig.1.5: Change in band-gap energy Eg with particle size.

Additionally, E_g is the band gap energy for the bulk semiconductor material. According to Eq.7, the effective band gap, the energy required by an electron to transfer from the highest valence

band energy to the lowest conduction band energy, increases with decreasing particle size. The Fig.1.5 shows the increasing bandgap energy and intra-band spacing with quantum confinement.

The quantum confinement effect is what allows the tuning of absorption and emission wavelengths over the entire visible spectrum as a function of quantum dot size. As is shown in Fig. 1.5 and 1.6, the density of states changes from being continuous at all energy levels for a bulk material to becoming discrete transitions at certain energy levels for the quantum dot.

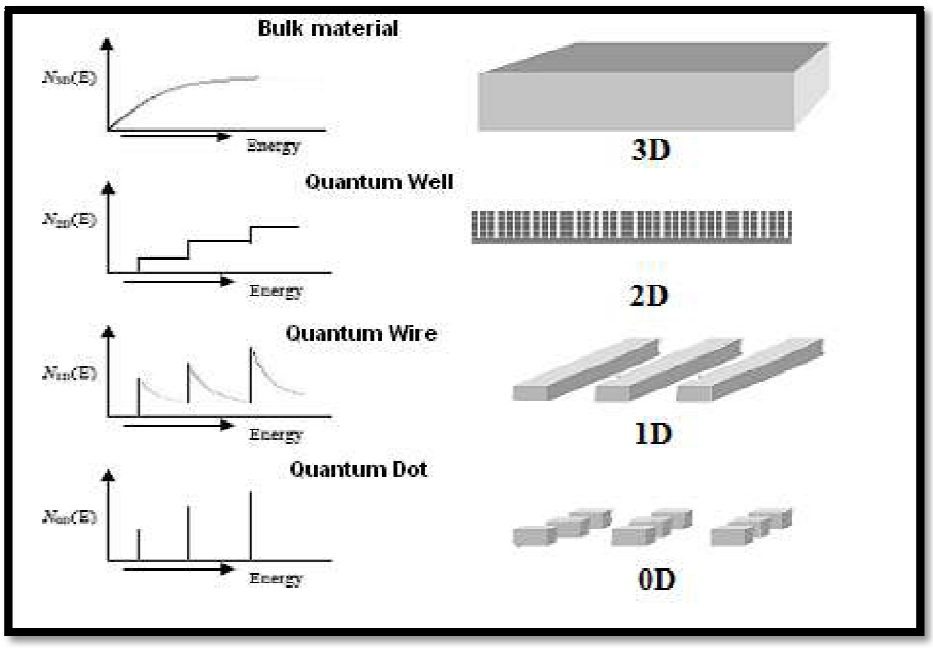

Fig.1.6: The progression of confinement and effects on the density of states

1.4 Advantage of Nanocrystalline Materials

Nanocrystalline materials have attracted tremendous interest in the chemistry and physics communities because of their novel properties. Nanocrystalline materials exhibit exceptional mechanical properties, representing an exciting new class of structural materials for technological applications. The advancement of this important field depends on the development of new fabrication methods, new characterization methods and an appreciation of the underlying nanoscale and interface effects. The first major identifiable activity in the field of nanocrystalline (or nanostructured, or nanophase) materials was reported in the early 1980s by Gleiter and coworkers 1, who synthesized ultrafine-grained materials by the in-situ consolidation of

nanoscale atomic clusters. The ultra-small size (< 100 nm) of the grains in these nanocrystalline materials can result in dramatically improved or different properties from conventional grain-size (> 1 μm) polycrystalline or single crystal materials of the same chemical composition. The differences were attributed to two main physical phenomena that become prominent as the material dimension changes from three dimensions (3D) to zero dimension (0D). These include classical mechanical effects 2, as well as quantum mechanical effects, for example the "quantum size effect" where the electronic and optical properties of solids are altered due to changes in the band structures. Additionally, the enhanced surface/volume ratio in nano dimensions forces more than 33% of the atoms to be on the surface (for 10nm dot 35), drastically altering the physical properties such as having lower melting temperature and lower sintering temperature, and higher diffusion force at elevated temperatures.

Electronic devices incorporating nanocrystalline materials are being extensively studied to exploit the unique electrical and optical properties that arise from "quantum-confinement" of charge carriers. A good example of the manipulation of optical properties is variation of emission spectra obtained from differen size Cadmium Selenide (CdSe)quantum dots.[30]

Fig. 1.7: The image above represents the fluorescent-emission colors of cadmium selenide nanocrystals, or "quantum dots," excited with a near-ultraviolet lamp.[30]

The excitation fluorescence depends on the nanocrystal size which is characteristic of the particle's band gap energy. As the physical dimensions of the particle become smaller, the band gap energy becomes higher. Therefore, different size particles of the same material have different band gaps and therefore emit different colors. Since particle size determines the optical and electrical properties, as demonstrated for CdSe, ability to produce monodispersed pure nanoparticles with a narrow size distribution is very important. The average size and the size distribution of the nanoparticles are largely determined by the technique that is used to produce them. Out of many techniques developed to fabricate nanoparticles, chemical precipitation techniques are the most suitable for producing narrow particle distributions.

Refrences

1. J. H. Zhao, A. H. Wang, M. A. Green and F. Ferrazza, Appl Phys Lett 73 (14),1991-1993 (1998).
2. T. M. L. Wigley and S. C. B. Raper, Science, 2001, 293, 451–454.
3. IEA, in Key World Energy Statistics, International Energy Agency, 2006.
4. N. S. Lewis, G. W. Crabtree, A. J. Nozik, M. R. Wasielewski and A. P. Alivisatos, in Basic Energy Sciences Report on Basic Research Needs for Solar Energy Utilization, Science, U.S. Department of Energy, 2005.
5. S. Dayal, N. Kopidakis, D. C. Olson, D. S. Ginley and G. Rumbles, Nano Lett., 2010, 10, 239–242.
6. S. Dayal, N. Kopidakis, D. C. Olson, D. S. Ginley and G. Rumbles, Nano Lett., 2010, 10, 239–242.
7. C. J. Brabec, N. S. Sariciftci and J. C. Hummelen, Adv. Funct. Mater., 2001, 11, 15–26.
8. Adam J. Moule, Lilian Chang, Chandru Thambidurai, Ruxandra Vidu and Pieter Stroeve, Journal Of material Chemistry, 2012, 22, 2351.
9. Kim, J.Y.; Lee, K.; Coates, N.E.; Moses, D.; Nguyen, T.Q.; Dante, M.; Heeger, A.J. Efficient tandem polymer solar cells fabricated by all-solution processing. Science 2007, 317, 222–225.
10. Kim, K.; Liu, J.; Namboothiry, M.A.G.; Carroll, D.L. Roles of donor and acceptor nanodomains in 6% efficient thermally annealed polymer photovoltaics. Appl. Phys. Lett. 2007, 90, 163511.

11. Marks, R.N.; Halls, J.J.M.; Bradley, D.D.C.; Friend, R.H.; Holmes, A.B. The photovoltaic
response in poly (p-phenylene vinylene) thin-film devices. J. Phys. Condens. Matter 1994, 6, 1379–1394.

12. Barth, S.; Basler, H. Intrinsic photoconduction in PPV-type conjugated polymers. Phys. Rev. Lett. 1997, 79, 4445–4448.

13. Grahn, H.T. Introduction to Semiconductor Physics; World Scientific Publishing Company: Singapore, 1999.

14. Gratzel, M. Dye-sensitized solar cells. J. Photochem. Photobiol. C 2003, 4, 145–153.

15. Boucle, J.; Ravirajan, P.; Nelson, J. Hybrid polymer-metal oxide thin films for photovoltaic
applications. J. Mater. Chem. 2007, 17, 3141–3153.

16. [Gledhill, S.E.; Scott, B.; Gregg, B.A. Organic and nano-structured composite photovoltaics: An overview. J. Mater. Res. 2005, 20, 3167–3179.

17. McGehee, M.D. Nanostructured organic-inorganic hybrid solar cells. Mater. Res. Soc. Bull. 2009, 34, 95–100.

18. Pang-Leen Ong and Igor A. Levitsky. Organic / IV, III-V Semiconductor Hybrid Solar Cells energies, ISSN 1996-1073, 2010

19. W. J. E. Beek, M. M. Wienk and R. A. J. Janssen, Adv Mater 16 (12), 1009-1013 (2004).

20. S. D. Oosterhout, M. M. Wienk, S. S. van Bavel, R. Thiedmann, L. J. A. Koster, J. Gilot, J. Loos, V. Schmidt and R. A. J. Janssen, Nat Mater 8 (10), 818-824 (2009).

21. W. J. E. Beek, M. M. Wienk and R. A. J. Janssen, Adv Funct Mater 16 (8), 1112-1116 (2006).

22. Z. A. Peng and X. G. Peng, J Am Chem Soc 123 (1), 183-184 (2001).

23. S. Zhang, P. W. Cyr, S. A. McDonald, G. Konstantatos and E. H. Sargent, Appl Phys Lett 87 (23), 233101 (2005).

24. A. Watt, E. Thomsen, P. Meredith and H. Rubinsztein-Dunlop, Chem Commun (20), 2334-2335 (2004).

25. A. A. R. Watt, D. Blake, J. H. Warner, E. A. Thomsen, E. L. Tavenner, H. Rubinsztein-Dunlop and P. Meredith, J Phys D Appl Phys 38 (12), 2006-2012 (2005).

26. C. Y. Liu, Z. C. Holman and U. R. Kortshagen, Nano Lett 9 (1), 449-452 (2009).

27. YUNFEI ZHOU "Bulk-heterojunction Hybrid Solar Cells Based on colloidal CdSe Quantum Dots and Conjugated Polymers" , dissertation 2011.

28. G. A. Prinz and J. H. Hathaway, Physics Today 48 (4), 24 (1995); P. Grünberg, Physics Today 54(5), 31 (2001); G. A. Prinz, Science 282, 1660 (1998).

29. D. Vanmaekelbergh and P. Liljeroth, Chem. Soc. Rev. 34. Page 299-312 (2005).

30. Yu. P. Rakovich, J. F. Donegan, S. A. Filonovich, M. J. M. Gomes, D. V. Talapin, A. L. Rogach, A. Eychmüller, Physica E , 17, 99-100.2003.

Material Review

CHAPTER- 2

2.1 PbSe Quantum Dots (QDs)

PbSe is a direct band gap semiconductor with a band gap of 0.28eV that corresponds to absorption wavelength of 4770nm. As a result of the long wavelength, PbSe nanoparticles found application in IR detectors. However, reducing crystal size to a few nanometers can bring the band gap into visible region. A PbSe QD diameter of 5.7nm will have a band gap of 0.72 eV, corresponding to absorption wavelength of 1720nm, compared to bulk of 0.28eV.[1]

While size tunability of QDs enable manipulation of the band gap, large Bohr radius (23nm) allows PbSe to provide an alternate way to change the band gap and quantum levels without having to decrease the QD size very much. This allows larger QD sizes to have higher photon absorption cross-sections. Also the equal effective electron and hole mass in PbSe allows strong quantum confinement, due to phonon bottle neck in both valance and conduction band, compared to other semiconductor materials such as Cadmium selenide, Indium phosphate, Gallium Arsenide etc.(Fig.2.1). This strong quantum confinement in the PbSe QDs provides a unique opportunity for electro-optical applications. Also researchers have shown that due to phonon bottle neck in both valance and conduction band, the Multiple Exciton Generation (MEG) in PbSe NCs is highly efficient, extremely fast, and occurs in wavelength range that has a potential to provide significantly increased solar cell power conversion efficiency.[1]

In bulk semiconductors, the absorption of one photon of energy greater than the bandgap leads to one electron-hole pair by losing the excess energy as heat through electron-phonon scattering and subsequent phonon emission, as the hot photo generated carriers (hot carrier) relax to their respective band edges (Fig. 1.3). The main approach to reduce this loss in efficiency has been to use a stack of cascaded multiple p-n junctions with band gaps better matched to the solar spectrum. In the limit of an infinite stack of band gaps perfectly matched to the solar spectrum, the ultimate conversion efficiency at one-sun intensity can increase to about 66%.[1]

Another approach is to use the hot carriers before they relax to the band edge via phonon emission.[1] There are two fundamental ways to use the hot carriers for enhancing the efficiency of photon conversion. One way produces an enhanced

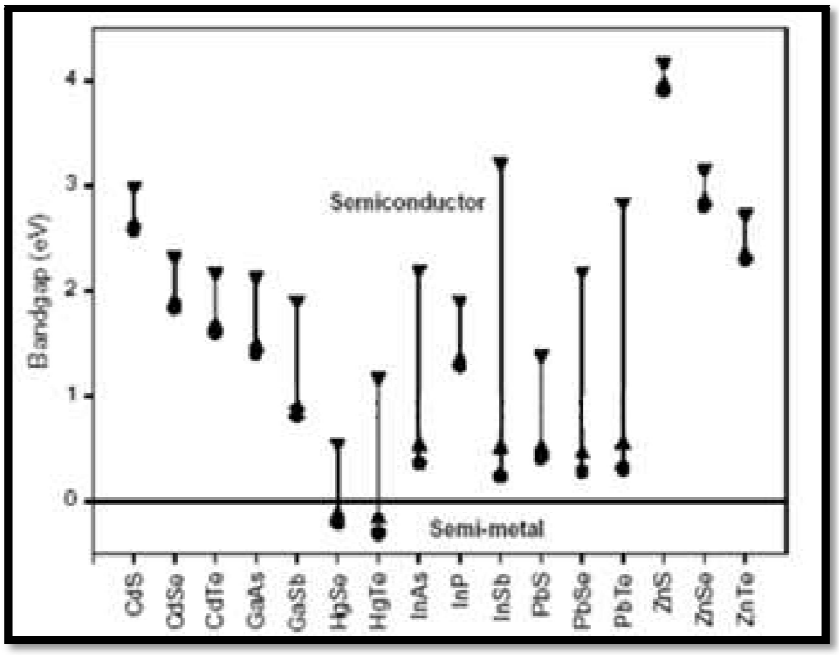

Fig 2.1: Band gap increment in various semiconductor QDs due to quantum confinement (from bulk to 3.9nm). {Taken from H. Weller, Pure Appl. Chem. 72,295 (2000)}

photovoltage, and the other way produces an enhanced photocurrent. The former requires that the carriers be extracted from the photo converter before they cool [1]. To achieve the enhanced photo voltage, the rates of photo generated carrier separation, transport, and interfacial transfer across the contacts to the semiconductor must all be fast compared to the rate of carrier cooling. The latter requires the energetic hot carriers to produce a second (or more) electron-hole pair (Fig.2.2). The formation of multiple electron-hole pairs per absorbed photon is a process explained by impact ionization (I.I.). In this process, an electron or hole with kinetic energy greater than the semiconductor band gap produces one or more additional electron-hole pairs. The kinetic energy can be created either by applying an electric field or by absorbing a photon with energy above the semiconductor band gap energy. In order to have efficient multiple exciton generation,[1] the rate of impact ionization has to be greater than the rate of carrier cooling and other relaxation processes for hot carriers.

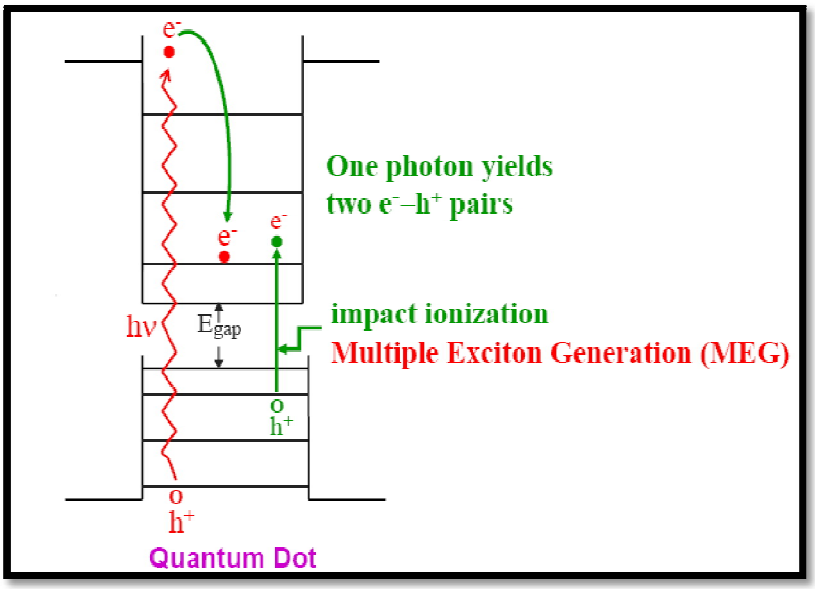

Fig 2.2: Multiple excitons generation of quantum dot PV solar cells (Taken from J. Nozik, NERL)

In quantum dots, the relaxation dynamics of photo generated carriers are largely affected by the quantization effects. The reason for that is, when the carriers in the semiconductor are confined by a potential barrier to a region of space that is smaller than or comparable to their deBroglie wavelength or to Bohr radius of excitons in the semiconductor bulk, the cooling rate of hot carriers is dramatically reduced, and the rate of impact ionization could become competitive with the rate of carrier cooling.[2] The threshold photon energy for multi exciton generation is given by

$$hv = \left(2 + \frac{m_e^*}{m_h^*}\right) E_g$$

where, m_e* and m_h* are electron and hole effective masses, respectively and E_g is the band gap of the quantum dot. If ,which is the case for PbSe , the excess energy of the initial exciton will be equally shared between the electron and the hole in generating the second e-h pair, and thus, the threshold energy for carrier multiplication is $\geq 3Eg$ [2]. For example, 9.5nm QD where band gap is .65eV can harvest maximum solar power according to the AM 1.5 solar spectrum shown in fig 2.3

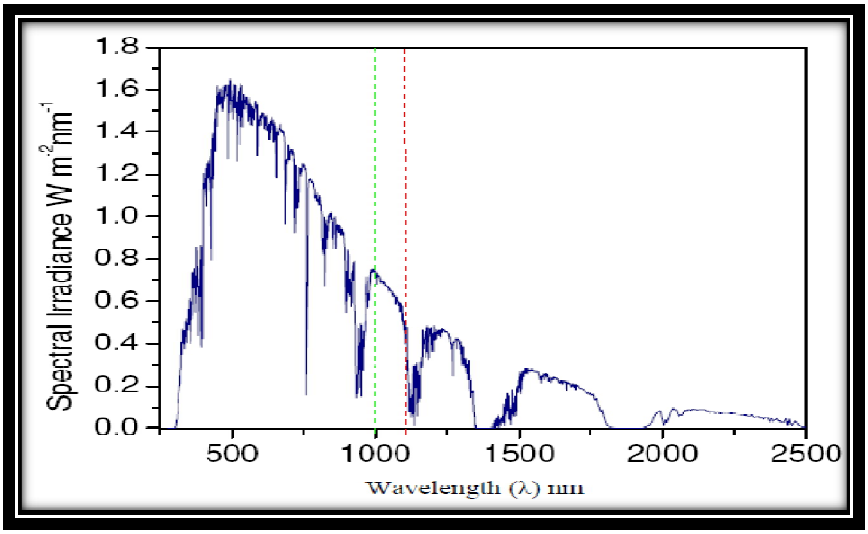

Fig.2.3: Air Mass (AM) 1.5 solar spectrum. The dashed lines in green and red represent limits of organic and silicon based solar cells, respectively. (Taken from: www.solems.com/Radiometry-basics)

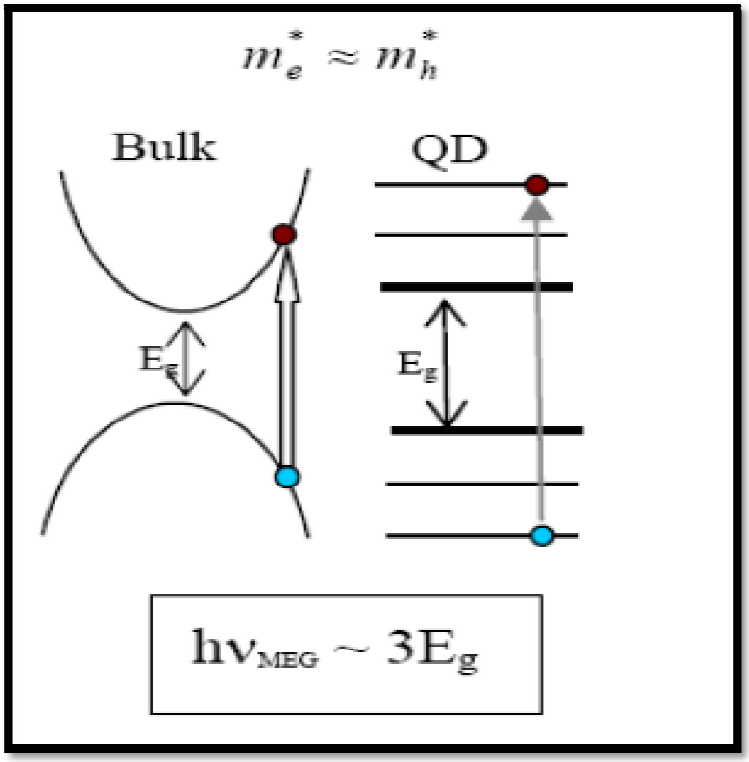

Fig 2.4: Comparison of energy levels and threshold energy for MEG in QDs for m_e*~ m_h*.

2.2. Exciton Dissociation

The success of electronic devices based on semiconductor quantum dots hinges on the ability to efficiently extract charge carriers from QD and to transport the carriers between electrodes. For example, in quantum dot photovoltaic devices, bound electron hole pairs (excitons) generated by light absorption must be dissociated and the resulting carriers must be collected by electrodes.[3] This mechanism depends on several properties of the interface between the QD and the transporting medium. (1) The coupling between QD and transporting medium must be strong enough to separate the electron-hole pairs either by charge transfer across the boundary or diffusing one exciton to the next medium prior to non-radiative Auger recombination. (2) Intimate contact between the QD and the transporting medium, which lowers the interface traps. (3) Large cross section area between the QD and transporting medium. (4) Built-in electric field between electrodes to drive the charges to electrodes. Polymer/QD composites have been recognized to posse both the attributes where charge separation is enhanced at interfaces and the electron and hole transport takes place in two different materials[4].The most important parameters that control exciton dissociation are; ionization potential, electron affinity, band gaps of polymer and QD, density of QDs, distribution of QDs within the polymer, and the nature of contact between polymer and QD. The effect of these parameters on exciton dissociation is discussed below.

Choice of the polymer is crucial for effective coupling between the QD and the polymer. In order for the holes in the QD to transfer into the HOMO level of the polymer, the ionization potential of the polymer must be less than that for the QD. Similarly, transfer of an electron in the LUMO level of the polymer to the QD is possible only if electron affinity of the QD is higher than that of the polymer. The range of diffusion for excitons in polymers is 5-15nm[4].

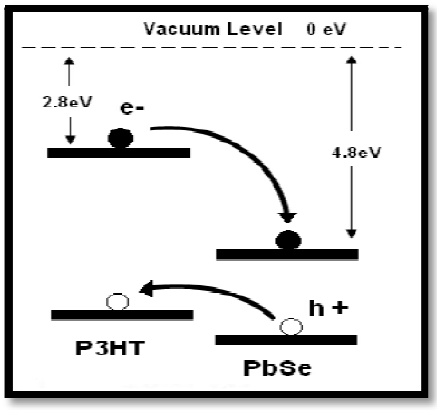

Fig.2.5: The schematic energy level diagram for PbSe nanodots and P3HT (polymer) showing the charge transfer of electrons to PbSe and holes to P3HT.

Only the excitons generated close to an interface can be dissociated. For this reason, density of QDs in the polymer plays a crucial role in dissociation of excitons in the polymer. Therefore, it is important to maintain an optimum density of QD for a given system for efficient dissociation process. Uniform distribution of QDs within the polymer is important to avoid formation of isolated QD aggregates surrounded by polymer.

Electrons accumulated in QD aggregates become trapped and eventually lead to carrier recombination. Such aggregation is readily observed in polymer/QD composites when surfactants are removed prior to mixing [5]. Therefore, the removal of surfactant has to happen just before the QDs are mixed with the polymer. Several chemical treatments including hydrazine (N_2H_4) treatment have been developed to remove the surfactant coating from QDs that are deposited on substrates[6]. However, to fabricate QD/host composite structures, chemical washing to remove surfactants has to be done prior to embedding them in the host, which inevitably leads to agglomeration and non-uniform distribution of the QDs in the host material. Therefore, washing-off of the organic surfactant using a hydrazine solution is not suitable to make a composite of quantum dots and polymers. In addition, toxicity of hydrazine is also a concern. The nature of the contact between the polymer and the quantum dot is important for fast dissociation. If QD makes an intimate contact with the polymer such that there is significant overlap of the wave functions between the two materials, tunneling of one charge carrier type of the exciton into the other material is energetically favorable[7]. This mechanism that is dominant in QDs without surfactants is known as the Dexter mechanism[7]. If there is a significant spectral

overlap between the emission and absorption spectrum of the two materials, a Coulomb dipole-dipole interaction promotes energy transfer between the two materials. This mechanism that is not hindered by the presence of an interfacial surfactant layer is known as the Forster mechanism.14 Exciton dissociation through Dexter and Forster mechanisms are shown in Fig. 1.14. [8,9]

According to the diagram in Fig 2.6, in order to have an efficient Forster mechanism, the band gaps of the QD and the polymer have to be in the same range. For example, single exciton dissociation in surfactant-coated CdSe nanoparticles (band gap 2.0-2.6 eV) and the polymer MEH-PPV (*poly[2-methoxy-5-(2'-ethyl-hexyloxy)-pphenylenevinylene*), band-gap ~2.1 eV, have been observed while such a transition is absent in MEH-PPV and surfactant coated QDs of CdS (band gap 2.6-3.1 eV)[7].

In order to have an efficient Dexter mechanism, the surfactant has to be removed from the quantum dot during the interaction. Efficient exciton dissociation between uncoated CdS and MEH-PPV has been observed due to the Dexter mechanism.[7] Finally, these results have led to the conclusion that for a polymer/QD composite where the band gaps of the two materials are far apart, presence of surfactants at the interface suppresses the exciton dissociation process. Therefore, one of the primary focuses of this project is to develop a method to deposit surfactant-free quantum dots on a substrate and to produce QDs/Polymer hybrid structure with direct contact between quantum dots and the polymer.

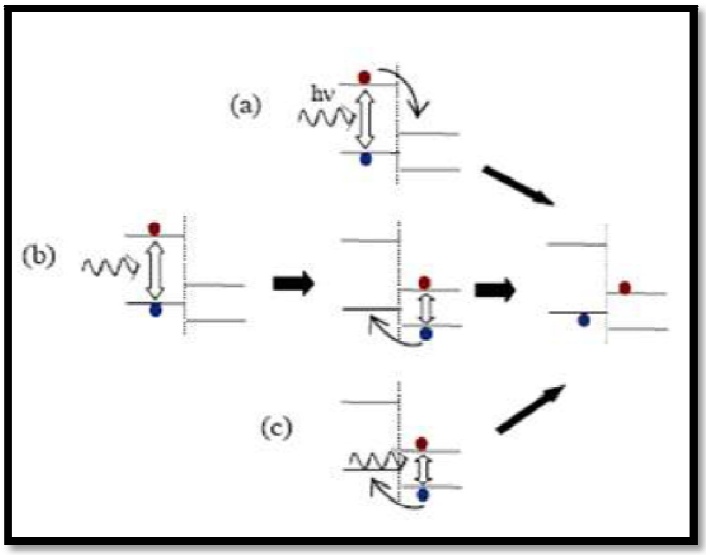

Fig.2.6: Possible paths for exciton dissociation in polymer/QD composites. (a) Generation of an exciton in polymer followed by electron transfer to QD by Dexter mechanism. (b) generation of an exciton in polymer followed by exciton transfer to QD by Forster mechanism. Exciton in QD can dissociate by transferring the hole to the polymer. (c) Generation of an exciton in QD and transfer of the hole to the polymer by Dexter mechanism.[10]

2.3 Core-Shell Structures

Colloidal core/shell nanocrystals contain at least two semiconductor materials in an onion like structure. The possibility to tune the basic optical properties of the core nanocrystals(NCs), for example, their fluorescence wavelength, quantum yield, and lifetime, by growing an epitaxial-type shell of another semiconductor has fueled significant progress on the chemical synthesis of these systems. In such core/shell nanocrystals, the shell provides a physical barrier between the optically active core and the surrounding medium, thus making the nanocrystals less sensitive to environmental changes, surface chemistry, and photo-oxidation. The shell further provides an efficient passivation of the surface trap states, giving rise to a strongly enhanced fluorescence quantum yield. Due to this effect, we can use nanocrystals in applications such as biological labeling and light-emitting devices, which rely on their emission properties [46]. On the other hand, the application of core-shell structures offer the potential to increase charge

separation yield, reduce recombination and enhance both V_{OC} and I_{SC} , resulting in more efficient devices. Figure 1 shows synthesis of core shell structure as an example.

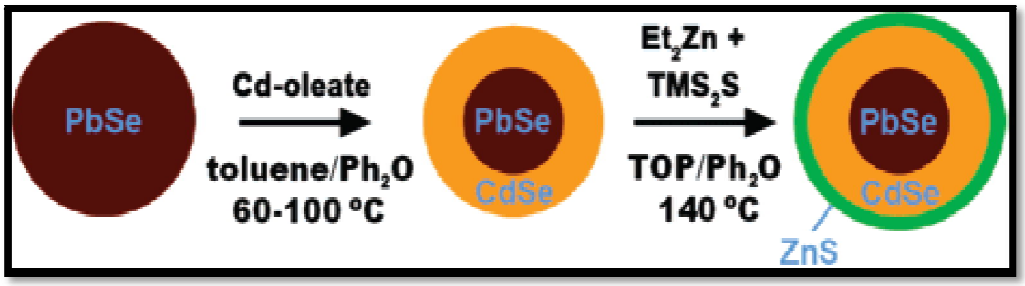

Figure 2.7 Synthesis of PbSe-CdSe and PbSe-CdSe-ZnS NQDs [2]

The size-dependent optical properties of NCs have been the focus of significant research over the past two decades. The nanometric crystal size also results in a very high surface-to-volume ratio. The co-ordination sphere of this high population of surface atoms partially occurs via complex formation with the stabilizing ligands. Nevertheless, a significant fraction of these organically passivated core NCs typically exhibit surface-related trap states acting as fast non-radiative de-excitation channels for photo generated charge carriers, thereby reducing the fluorescence quantum yield (QY).An important strategy to improve NCs' surface passivation is their overgrowth with a shell of a second semiconductor, resulting in core/shell (CS) system. In this manner, the fluorescence efficiency and stability against photo-oxidation of various types of semiconductor NCs has seen significant improvement. Furthermore, by the appropriate choice of the core and shell materials, it is possible to tune the emission wavelength in a larger spectral window than with both materials alone.

2.3.1 Classification of Core/Shell Systems

Depending on the band gaps and the relative position of electronic energy levels of the involved semiconductors, the shell can have different functions in CS NCs. Three cases can be distinguished, denominated type-I, reverse type-I, and type-II band alignment (Figure 2.8).

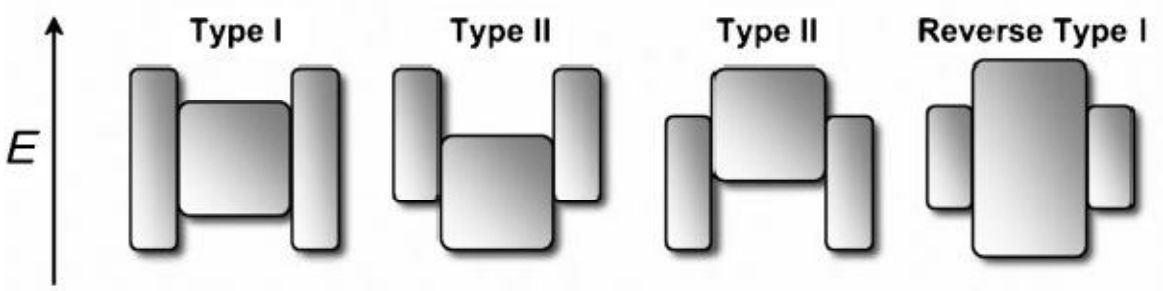

Figure 2.8. Schematic representation of the energy-level alignment in different core/shell systems realized with semiconductor NCs to date. The upper and lower edges of the rectangles correspond to the positions of the conduction- and valence-band edge of the core (center) and shell materials, respectively.

In type I the band gap of the shell material is larger than that of the core and both electrons and holes are confined in the core. In the type II, the band gap of the shell material is smaller than that of the core and, depending of the thickness of the shell, the holes and electrons are partially or completely confined in the shell. In the reverse type I, either the valence-band edge or the conduction-band edge of the shell material is located in the band gap of the core. Upon excitation of the NC, the resulting staggered band alignment leads to a spatial separation of the hole and the electron in different regions of the CS structure.[11]

2.3.2 General considerations for the design of core/shell systems

(A). Choice of the Shell Material

A general requirement for the synthesis of CS NCs with satisfactory optical properties is epitaxial-type shell growth. Therefore an appropriate band alignment is not the sole criterion for the choice of materials but rather the core and shell materials should crystallize in the same structure and exhibit a small lattice mismatch. In the opposite case, the growth of the shell results in strain and the formation of defect states at the core/shell interface or within the shell. These can act as trap states for photo generated charge carriers and diminish the fluorescence QY.[11]

(B). Precursors for Shell Growth

Appropriate precursors for shell growth should fulfill the criteria of high reactivity and selectivity (no side reactions).For practical reasons, and in particular if the scale-up of the production process is sought, additional properties of the precursors come into play. Pyrophoric and/or highly toxic compounds require special precautions for their manipulation, especially if used in large quantities.

(C). Control of the Shell Thickness

The control of the shell thickness is a delicate point in the fabrication of CS NCs and deserves special attention. If the shell is too thin, the passivation of the core NCs is inefficient, resulting in reduced photo stability. In the opposite case, the optical properties of the resulting CS NCs generally deteriorate as a consequence of strain induced by the lattice mismatch of the core and shell materials, accompanied by the generation of defect states.[11]

2.3.3 Characterization of CS Systems

Most of the basic characterization techniques for CS systems are also applied to investigate core NCs, such as UV/Vis and PL spectroscopy, powder X-ray diffraction or transmission electron microscopy (TEM). In the case of CS NCs, however, several experimental difficulties may arise in proving successful shell growth. Optical properties, generally extremely sensitive to NC surface modification, can only give indirect information about the possible overcoating with a shell and therefore spectroscopic analyses (UV/Vis, PL) must be completed by structural studies. The increase of the NCs'diameter revealed by TEM or -esolution (HR) TEM is considered to be the most direct proof of successful shell growth. Nevertheless, an accurate determination of the size difference before and after addition of the shell can be severely limited or even impossible by TEM depending on the materials used, the size and size distribution of the core NCs,as well as the shell thickness. Advanced microscopy techniques including scanning transmission electron micro-scopy (STEM) coupled with electron energy loss spectroscopy (EELS) or with energy-dispersive X-ray spectroscopy (EDX) can give valuable insight into the obtained CS structures. As an example, the former technique has been applied to characterize CdSe/ZnS CS NCs, revealing a highly anisotropic distribution of the shell material around the core NCs.[11]Among other, more sophisticated characterization methods for CS NCs, X-ray

photoelectron spectroscopy (XPS) should be cited. This method is a powerful tool to simultaneously investigate the core/shell interface, the shell thickness, and even the NCs' surface properties, such as the binding modes of surface ligands.[11]

2.4 Alloy Nanostructures

An alloy is a phase comprising of one or more components. There distinguish three of alloys:

(a)Substitutional: solute substitutes the solvent in the crystal lattice without structural changes.

(b)Interstitial: solute does not occupy the sites in the lattice of the solvent but resides in crystallographic pores.

(c)Transformational: A completely new lattice is formed. Usually occurs as a result of intermetallic compound formation.

In substitutional solid solution, the arrangement of the solute atoms may be disordered (random) or ordered.

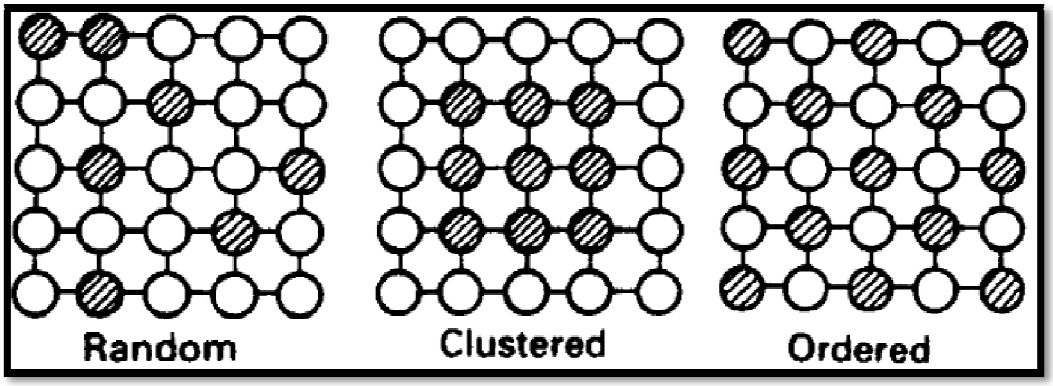

Figure 2.9: Arrangement of atoms in substitutional solid solution

Some alloy systems exhibit complete solid solubility (e.g. Cu-Ni, Cd-Mg), others show only limited solubility at any temperature. Several factors determine the limits of solubility. These are expressed as a series of rules often called William Hume-Rothery Rules. These are:

(1) Hume-Rothery Rule 1: Atomic Size Factor (the 15%) Rule.

Extensive substitutional solid solution occurs only if the relative Difference between the atomic diameters (radii) of the two species is Less than 15%. If the difference > 15%, the solubility is limited. Comparing the atomic radii of solids that form solid solutions, the Empirical rule given by Hume-Rothery is given as:

$$Mismatch = \left(\frac{r_{solute} - r_{solvent}}{r_{solvent}} \right) \times 100 \leq 15\%$$

(2)Hume-Rothery Rule 2: Crystal Structure Rule.

For appreciable solid solubility, the crystal structures of the two elements must be identical.

(3)Hume-Rothery Rule 3: Valency Rule.

A metal will dissolve a metal of higher valency to a greater extent than one of lower valency. The solute and solvent atoms should typically have the same valence in order to achieve maximum solubility.

(4)Hume-Rothery Rule 4: The Electro negativity Rule.

Electro negativity difference close to 0 gives maximum solubility. The more electropositive one element and the more electronegative the other, the greater is the likelihood that they will form an intermetallic compound instead of a substitutional solid solution. The solute and the solvent should lie relatively close in the electrochemical series.

2.4.1 Vegard's law

Vegard's law has been used extensively in mineralogy, metallurgy and materials science for the past six decades. According to the law, unit cell parameters should vary linearly with composition for a continuous substitutional solid solution in which atoms or ions that substitute for each other are randomly distributed. The simplest mathematical expression for Vegard's law for a binary solid solution A-B is:

$$a = a_A^o (1-X) + a_B^o (X) \quad (1)$$

where X = X_B is the mole fraction of component B and and a_A^o and a_B^o :

are the lattice parameters of pure components A and B respectively.

References

1. .A. S. Edelstein and R. C. Cammarata, Nanomaterilas: Synthesis, Properties an Applications.

2. .A. Marti, G. L. Araujo, Sol. Energy Mater. Sol. Cells, Vol.43, 203-222 (1996).

3. R. D. Schaller, M. A. Petruska, and V. I. Klimov, Applied Phys. Lett. 87, 253102(2005).

4. C.A. Leatherdale, C.R. Kagan, N.Y. Morgan, S.A. Empedocles,M.A. Kastner, andM.G. Bawendi, *Phys. Rev. B 62, 2669* (2000).

5. .A. Franceschetti and A. Zunger, *Phys. Rev. Vol 63, 153304* (2000).

6. M.Tamborra, M. Striccoli, R. Comparelli, M. L. Curri, A. Petrella and A. Agostiano, *Nanotechnology, Vol. 15, S240–S244* (2004).95

7. S. J. Kim, W. J. Kim, Y. Sahoo, A. N. Cartwright and P. N. Prasad, *App. Phys. Lett, 92, 031107* (2008).

8. J.H. Warner, A. R. Watt, E. Thomsen, N. Heckenberg, P. Meredith, and H. Rubinsztein-Dunlop, *J. Phys. Chem. B., Vol 109, Page 9001-9005* (2005).

9. N. Greenham, X. Peng, and A. Alivisatos, *Phys. Rev. B, 54, 17628* (1996).

10. Yu. P. Rakovich, J. F. Donegan, S. A. Filonovich, M. J. M. Gomes, D. V. Talapin, A. L. Rogach, A. Eychmüller, *Physica E , 17, 99-100*.2003

11. Peter Reiss, Myriam Protie `re, and Liang Li small 2009, 5, No. 2, 154–168

Nanoparticle Synthesis and Characterization Techniques

Chapter- 3

3.1 Nanoparticle Synthesis

Currently, there are several different techniques available for nanoparticle growth that include sol-gel processing , chemical synthesis , chemical vapour deposition (CVD) . Chemical synthesis permits the manipulation of matter at the molecular level. Because of mixing at the molecular level, good chemical homogeneity can be achieved. Also, by understanding the relationship between how matter is assembled on an atomic and molecular level and the resulting macroscopic properties, molecular synthetic chemistry can be tailored to prepare novel compounds.

3.1.1 Synthesis of core shell structure using SILAR process

Monodisperse colloidal PbSe QDs with high quantum yield were synthesized using literature's method [1]. Two solutions were prepared for CdSe shell growth. A cadmium injection solution (0.04 M) was prepared by heating cadmiumcyclohexanebutyrate (0.1804 g) in oleyamine (8.130 g) at 60?C under N_2 flow to obtain a clear colorless solution. A selenium injection solution (0.04 M) was prepared by mixing selenium powder (0.0316 g) in octadecene (7.880 g) at 220?C under N_2 flow until a clear yellow solution was obtained. Both injection solutions were later used at room temperature. For a typical shell formation,PbSe QDs (4.8 nm in diameter, 1.01 9 10-4mmol of particles [2]) dispersed in 5 ml of hexanes were loaded into a 25-ml three-neck flask and mixed with 1.500 g of octadecylamine and 5.000 g of octadecene. A mechanical pump was employed at room temperature for 30 min to remove hexanes from the flask. Subsequently, the reaction mixture was heated to 120 □C under N_2flow. Then, the predetermined amounts of the cadmium and selenium solutions were alternatively injected into the three-neck flask drop by drop with syringes using standard air-free procedures. The reaction time for each anion and cation layer was 10 min. The reaction was stopped by the injection of room-temperature toluene.

By employing the ‘‘successive ion layer adsorption and reaction (SILAR)’’ technology to form air-stable PbSe/CdSe QDs with strong photoluminescence.The quantum yield of PbSe/CdSe QDs was 70%.

3.1.2 Partial Cation Exchange method for core shell synthesis

All syntheses were performed under exclusion of air and moisture using standard Schlenk techniques up until reaction quenching.[3]

PbSe Cores: A 0.65 g (2.9 mmol) amount of PbO, 2.7 mL (8.5 mmol) of oleic acid,3 mL of trioctylphosphine (TOP), and 4 mL of phenyl ether were heatedto 150°C with stirring under flowing Ar for 90 min. The temperature was increased to 205°C, and 2 mL of a 2 M solution of TOPSe inTOP and ∼0.05 mL (i-Bu)2PH were rapidly injected. The reaction was quenched after 100 s by removal from heat and injection of cold toluene(∼10 mL) and then hexane (∼5 mL). PbSe NQDs were collected by precipitating with 15 mL of methanol followed by centrifugation and removal of the decantate. The very dark brown NQD solids were redispersed in ∼8 mL of hexane, and a portion was set aside for spectroscopy and other analyses. Before CdSe shell growth, the cores were washed one additional time by precipitating by addition of 5 mL of acetone and 5 mL of methanol, centrifugation, and removal of the decantate. Approximately 100 mg of solid product was formed.

CdSe Shell:A 1.5 g (11.7 mmol) amount of CdO, 9 mL (28.3 mmol)of oleic acid, and 22 mL of 1-octadecene were heated to 255 °C underAr until all of the CdO had dissolved. The clear solution was cooled to ∼120 °C under Ar flow to remove water. A 90 mg amount of PbSe cores from above was dispersed in 10 mL of toluene and degassed by Ar flow for ∼30 min. Immediately after the temperature of the PbSe solution was set to 100 °C, the cadmium oleate solution was added via cannula with stirring. Aliquots were removed and cooled by mixing with hexane, and NQDs were isolated and collected in a manner similar to that used for PbSe cores.

This is different from SILAR' s method as it is a novel method which takes advantage of the reactivity of PbSe NQD surface to produce PbSe/CdSe core/shell NQDs. Rather than exposing PbSe cores to both cadmium and selenium precursors, only cadmium was introduced and in excess relative to lead. Because heating PbSe in solution can cause observable Ostwald ripening at temperatures as low as 80 °C, it was expected that lead ions in the NQDs, especially those near the surface, would be susceptible to exchange with other metal ions from the solution. It was also expected that the excess cadmium and larger lattice energy of CdSe of 797 vs 730 kcal/mol would favor a net replacement of lead with cadmium over the reverse process.

Both processes above involve two pot synthesis and both of them are widely used for core shell formation.

3.2 Characterization Techniques used during work

A combination of microscopic and spectroscopic techniques was used to characterize the semiconductor nanomaterials prepared by the new methods. We have employed X-ray diffraction (XRD) and for the structural determinations. The optical and electronic properties of the nanomaterials were probed by UV-Visible, Photoluminescence (PL) and Fourier transform infrared (FTIR) spectroscopy. Furthermore, the morphology of the nanoparticles is viewed under Transmission Electron Microscope (TEM) and Scanning Electron Microscopy(SEM). Detailed description of these techniques is provided in the following sections.

3.2.1 X-ray Diffraction

X-ray diffraction (XRD) is a versatile, non-destructive analytical technique for identification and quantitative determination of the various crystalline forms, known as 'phases' of compounds present in powdered and solid samples. The result of an XRD measure is a XRD pattern or diffractogram, showing phases present (peak positions), phase concentrations (peak heights), amorphous content (background bump) and crystallite size/strain (peak widths).

Identification is achieved by comparing the diffractogram obtained from an unknown sample with an internationally recognized database containing reference patterns. Modern computer-controlled diffractometer systems use automatic routines to measure, record, and interpret the unique diffractograms produced by individual constituents in even highly complex mixtures.

Theory A crystal lattice is a regular 3-dimensional distribution of atoms in space. These are arranged so that they form a series of parallel planes separated from one another by a distance d, which varies according to the nature of the material. For any crystal, planes exist in a number of different orientations, each with its own specific d-spacing.

When a monochromatic X-ray beam with wavelength λ is incident on lattice planes in a crystal at an angle θ, diffraction occurs only when the distance travelled by the rays reflected from successive planes differ by a complete number n of wavelengths. By varying the angle θ, the

Bragg's law (n λ = 2d sinθ) (Fig. 3.3) conditions are satisfied by different d-spacings in polycrystalline materials [4].

Plotting the angular positions and intensities of the resultant diffraction peaks produces a pattern which is characteristic of the sample. Where a mixture of different phases is present, the diffractogram is formed by addition of the individual patterns.

Utility of XRD for Nanomaterials

Many structural properties of the nanostructures such as crystalline phase, particle size and structure evolution in Bragg planes, macroscopic stress/strain etc. can be revealed with the help of XRD. But here we shall mention few aspects directly relevant to our work.

Crystal identification: Since we have attempted new methods to prepare nanomaterials, it is of immense importance to identify these materials. With the help of XRD data we can check the amorphous or crystalline nature of the newly formed material. If the prepared material is crystalline, we can determine its basic lattice structure (e.g. cubic or hexagonal etc.) by indexing its lattice planes. One can also determine the changes in various lattice parameters of a particular bulk and nanosized material.

Crystallite size: A perfect crystal would extend in all directions to infinity, so we can say that no crystal is perfect due to its finite size. This deviation from perfect crystallinity leads to a broadening of the diffraction peaks. However, above a certain size (100-500 nm) this type of broadening is negligible.

Scherrer (1918) first observed that small crystallite size could give rise to line broadening. He derived a well- known equation for relating the crystallite size to the broadening, which is called 'Debye-Scherrer Formula' [5]:

$$Dv = \frac{k\lambda}{\beta Cos\theta} \qquad \{3.1\}$$

Where, the symbols represent the following parameters:

D_v = Volume weighted crystallite size. D is the 'average' dimension of the crystallites normal to the reflecting planes. We call it 'average' because the x-ray beam irradiates a large number of crystallites, so that the value of D obtained represents the mean value of the actual size distribution present. λ = wavelength of the radiation. k = Scherrer constant. k varies from 0.89 to 1.39, but for most cases, is close to 1. Since the precision of crystallite size analysis is, at best, of the order of ± 10 %, the assumption of k=1 in (3.1) is generally justifiable for irregular shapes of crystallites. β = the integral breadth of a reflection (in radians 2θ) located at 2θ commonlyconsidered as the full width at half maxima (FWHM) in radians for a certain peak

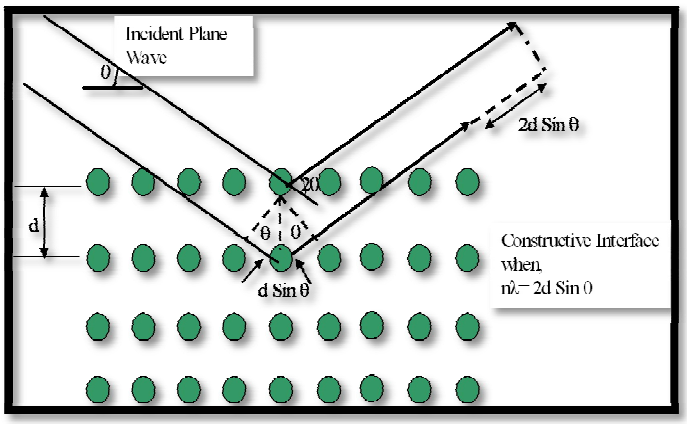

position

Figure 3.1: Schematic diagram showing Bragg diffraction from a set of planes

Crystallite size is a measure of the size of a coherently diffracting domain. Due to the presence of polycrystalline aggregates, crystallite size is not generally the same thing as particle size. When crystallites are less than approximately 100 nm in size, appreciable broadening in the x-ray diffraction lines will occur. These regions may, in fact, correspond to the actual size of the particles. At other times, however, these regions form 'domains' in a larger particle and may be a distinguishing and important feature. In either case, the observed line broadening can be used to estimate the average size. In the simplest case where the particles are stress-free, the size is estimated from a single diffraction peak. But in cases where stress may be present, a more robust method involving several diffraction peaks is required.

Instrumental Details

In an X-ray experiment, diffracted intensity is recorded as a function of the diffracted angle. All the reported XRD scans were taken on a Phillips X'pert diffractometer using a diffracted beam monochromator PW3123/10 for Cu $K_{\alpha}1$ radiation (λ = 1.54056Å) from a rotating anode x-ray generator operating at 40kV (generator tension) and 30mA (generator current). A CPS 120 detector with Si (a= 0.543088nm) was used as an internal standard to record the patterns. Data has been collected normally at the scan rate of 2°-3° per minute keeping both incident and diffraction beam anti-scatter slit fixed at 1° with slit angle 1°.

Samples Used and Their Preparation

All the diffractograms reported are for powder samples. Normally we have made powder films from colloidal suspension of nanoparticles by the spin coating procedure. In this method we deposit the drops of the suspension with the help of a micropipette on a clean glass substrate which is slowly spinning. Spin motion of substrate considerably helps in uniform distribution of particles and prevents agglomeration of nanoparticles. Drops are deposited at a regular interval in order to obtain a uniform film. XRD patterns are recorded only when the sample is completely dry.

3.2.2 UV-Visible spectroscopy

Optical spectroscopy is one of the powerful tools for the characterization of nanomaterials, in general and semiconductor nanocrystallites, in particular. The absorption of ultraviolet/visible radiation by a molecule leads to transitions among the electronic energy levels of the molecule, and for this reason optical spectroscopy is alternately known as electronic spectroscopy. An absorption spectrum is a plot of the changes in absorption intensity against wavelength.

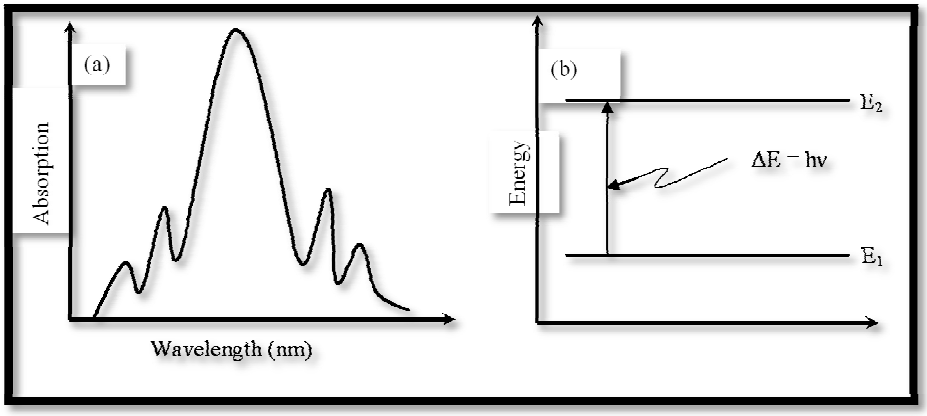

Figure 3.2: (a) A typical absorption spectrum (b) absorption involving two energy states E_1 and E_2.

The energy transition $E_1 \rightarrow E_2$ corresponds to the absorption of energy exactly equivalent to the energy of wavelength absorbed (Fig. 2.4).

{3.2}
$$\Delta E = (E_2 - E_1) = \frac{hc}{\lambda} = h\upsilon$$

A molecule can only absorb a particular frequency, if there exists, within the molecule an energy transition of magnitude $\Delta E = h\nu$. Wavelength range of the radiation absorbed for UV-Visible spectroscopy is 190- 800 nm (190-400 nm for UV and 400-800 nm for visible) which basically causes the changes in the electronic energy levels within the molecules. Practically we would be concerned with the absorptions above 200 nm because below 200nm oxygen present in the air begins to absorb strongly. The region below 200 nm is required for studying bond energies, etc. and therefore, usually referred as the vacuum ultraviolet [6].

Theory

Laws of Light Absorption – Beer's and Lambert's Laws:

These two early empirical laws govern the absorption of light by molecules. Beer's law relates the absorption to the concentration of absorbing solute, and Lambert's law relates the total absorption to the optical path length. In other words the Beer-Lambert law (also called the Beer-Lambert-Bouguer law or simply Beer's law) is the linear relationship between absorbance and concentration of an absorber of electromagnetic radiation. The general Beer-Lambert law is usually written as:

{3.3}
$$A = a_\lambda \times b \times c$$

Where, A is the measured absorbance, a_λ is a wavelength-dependent absorptivity coefficient, b is the path length, and c is the analyte concentration. When working in concentration units of molarity, the Beer-Lambert law can be written as:

{3.4} $$A = \varepsilon_\lambda \times b \times c$$

where ε_λ is the wavelength-dependent molar absorptivity coefficient with units of $M^{-1}cm^{-1}$. The λ subscript is often dropped with the understanding that a value for ε is for a specific wavelength. If multiple species that absorb light at a given wavelength are present in a sample, the total absorbance at that wavelength is the sum due to all absorbers:

{3.5} $$A = (\varepsilon_1 \times b \times c_1) + (\varepsilon_2 \times b \times c_2) + ...$$

Experimental measurements are usually made in terms of transmittance (T), which is defined as:

$$T = \frac{P}{P_0} \qquad \{3.6\}$$

where P is the power of light after it passes through the sample and Po is the initial light power. The relation between A and T is:

{3.7} $$A = -\log(T) = -\log\left[\frac{P}{P_0}\right]$$

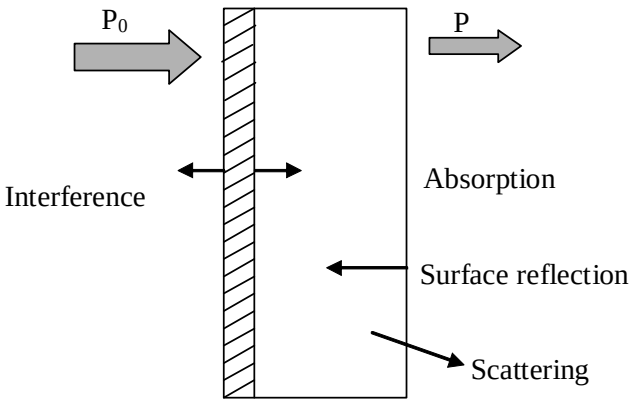

Figure 3.3: Various processes involved during the interaction of light with an optical filter.

Fig. 3.5 shows the case of absorption of light through an optical filter and includes other processes that decrease the transmittance such as surface reflectance and scattering. The linearity of the Beer-Lambert law is limited by chemical and instrumental factors.

Utility of UV-Visible Spectroscopy for Nanomaterials

An idea about the optical properties of any material can be obtained by its UV-Visible spectroscopy. The information about the changes in electronic energy levels within the molecule can thus be deduced. Researchers active in the field of nanomaterials have been employing the potential of UV-Visible spectroscopy for the investigation of band gap properties, particle size estimation and particle size distribution and so on [7]. UV-Visible spectrum of any nanomaterial is different from its bulk counterpart. Band gap, for example, of nanoscale material is greater than those in the corresponding bulk material. The reason being quantum confinement effects which dominate in the case of nanomaterials. Generally a blue shift of band gap is observed in the case of nanomaterials. Moreover, we can have an idea about the size distribution of nanostructures depending upon the nature of peak, shoulder or edge. For example, smaller is the peak width, narrower is the size distribution of nanoparticles and vice versa. In our work, we have extensively used UV-Visible spectroscopy to characterize the semiconductor nanostructures to understand the change in band gap and band structure due to quantum mechanical confinement.

Instrumental Details

Basically the modern UV-Visible spectrometer consists of a light source, double beams (reference and sample beams), a monochromator, a detector and amplification and recording devices. Schematic layout of an UV-Visible Spectrometer has been depicted in Fig. 3.6. UV light (λ<400nm) can be detected on photographic film or in a photoelectric cell. The source usually incorporates a tungsten filament lamp for wavelengths greater than 375nm, a deuterium lamp for values below that, and a solenoid-operated mirror, which automatically deflects light from either one as the machine scans through the wavelengths. The detector is usually a photomultiplier (photomultiplier R-928 in our case), and the ratio of reference beam to sample beam intensities (I_0/I) is fed to a pen recorder (the optical null technique is not used). The

recorder trace is invariably absorbance (A) against wavelength (λ) and photometric recording range for absorbance is 4 ~ 5 abs in the instrument used by us.

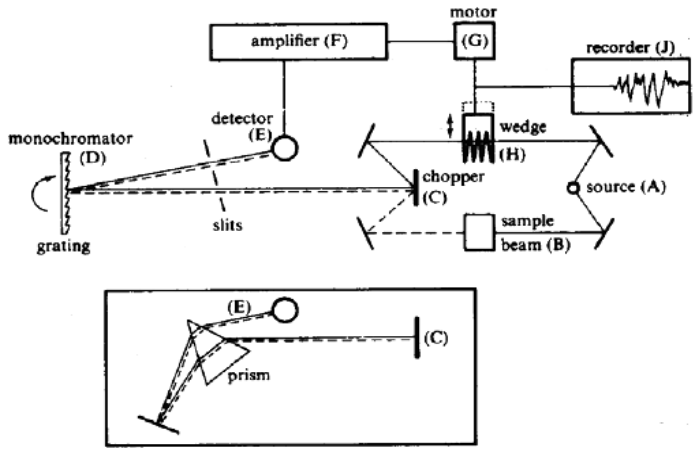

Figure 3.4: Schematic layout of an UV-Visible spectrometer. Main diagram – grating optics; inset – prism monochromatic, which can replace the grating [6].

For the present study of nanomaterials, we have used the model UV-2401PC UV-Visible spectrophotometer manufactured by Shimadzu Corporation, Kyoto, Japan. This spectrometer is operational at room temperature. Photometric system in this instrument is a double beam, direct ratio-measuring system employing the dynode feed-back method. With summing feed-back system, negative absorbance or more than 100% transmittance/reflectance can be accurately measured. The allowed wavelength range for this machine is 190-1100 nm (effective scanning range 190-900 nm). The halogen lamp for visible region and deuterium lamp for UV region are built in. Typically the deuterium lamp acts as a source for 190 nm to light source switching wavelength and the halogen lamp ranges from light source switching wavelength to 900 nm. For data acquisition we have normally selected a slit width of 1.0 nm while the chosen value of sampling interval is 0.1 nm. Resolution of this instrument is 0.1 nm.

Samples Used and Their Preparation

Both colloidal suspensions and powder samples of nanomaterials were characterized by the UV-Visible spectrophotometer. For liquid solutions, quartz cuvettes of path length 1cm were used as the sample keeping cells. Utmost care was exercised, while cleaning the cells. The optical

surfaces of the cell are never touched by hand. The cuvettes are cleaned with DI water and acetone. These are wiped with soft tissues dipped in methanol. For advanced cleaning, we carried out the entire cleaning procedure inside an ultrasonic bath. Sonication helps in scrubbing-off the firmly stuck dirt on the surface of cuvettes. In order to avoid the saturation of absorption intensity, we have usually acquired the UV- visible spectra for dilute solutions.

3.2.3 Photoluminescence Measurements

Photoluminescence (PL) spectroscopy is one of the most robust tools to study optical properties of semiconductors. A wealth of literature is available on the luminescent behavior and band structure of semiconductor nanostructures, in general and CdSe & other II-VI semiconductor nanoparticle. Optical properties of a material arise due to various transitions occurring within its band structure and can be elucidated with the help of a PL study.

Theory

A typical PL experiment in semiconductor can be divided into three stages: Firstly, the sample is excited from ground state, which is a completely filled valence band (VB) to the empty conduction band (CB). Energy pumped for excitation is $\hbar\omega$ pump. The laser creates electron-hole pairs due to a transfer of electrons from VB into CB. Secondly, the non-equilibrium electron and hole distributions tend to relax into the ground state. The initial intraband relaxation is caused by energy transfer to the crystal lattice, i.e. a step by step excitation of lattice vibration. Finally, the electron-hole pair recombines accompanied by the emission of light which is a photoluminescence process (Fig. 3.7).

Due to attractive Coulomb interaction between the charge carriers, the emission does not only contain contributions from states at or above the fundamental energy gap (E_{gap}) but also sharp discrete lines (transitions) just below E_{gap}, which originates from bound excitonic states [8].

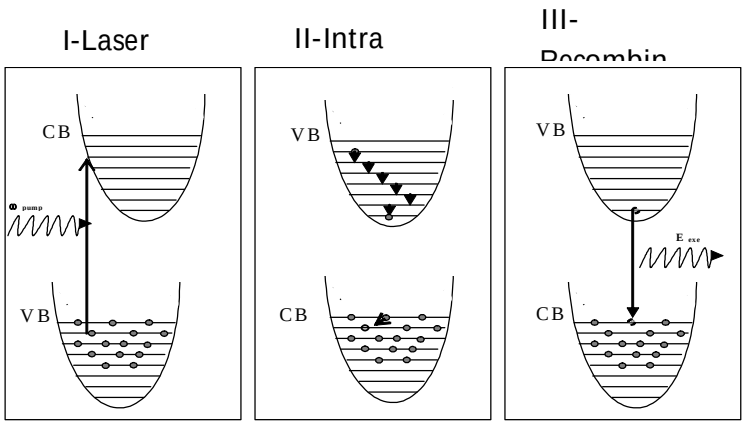

Figure 3.5: Sketch of the basic processes involved in a typical luminescence experiment in optically excited semiconductors.

Utility of PL Spectroscopy for Nanomaterials

The technique of photoluminescence (PL) has become a standard tool for obtaining information on the nature of nanostructures such as quantum dots. In bulk materials the luminescence often resembles a standard direct absorption spectrum, so there is little advantage in studying the details of both. High photon excitation energies above the band gap can be most effective for luminescence studies of bulk materials, but it has been found that for the case of nanoparticles the efficiency of luminescence decreases at high incoming photon energies. Non radiative relaxation pathways can short-circuit the luminescence at these high energies, and it is of interest to investigate the nature of these pathways [9].

Instrumental Details

PL is a static process in which input energy for excitation is fixed and output is varied i.e. response (PL emission intensity) is recorded for all available range of λ. The PL was measured using a home assembled system (Fig. 3.8), consisting of a two stage monochromator, a photomultiplier tube (PMT) with a lock-in amplifier for PL detection, and an Ar^+ ion laser operating at 488 nm and 5mW (corresponding to 0.125 Wcm^{-2}) for excitation in all measurements. An optical chopper and a lock-in amplifier were employed to lock the whole system at a particular frequency. The entire system was automated with a desktop computer and an interface card was used for interfacing the experiment with the computer.

Figure 3.6: Perkin Elmer LS 55 fluorescence spectrometer.

Samples Used and Their Preparation

Samples used for PL experiments are the same as those prepared for UV-Vis experiments (Refer UV-Vis Absorbance sample preparation section: 3.2.2).

3.2.4 Fourier Transform Infrared Spectroscopy

Fourier transform Infrared (FTIR) spectroscopy is an important tool for the identification of compounds and can be used in conjunction with other methods, such as UV and NMR spectroscopy, or alone to quickly establish the presence or absence of certain structural/functional groups in a molecule [10]. One can also use the unique collection of absorption bands to confirm the identity of a pure compound or to detect the presence of specific impurities.

Theory

Fourier Transform Infrared (FTIR) Spectroscopy bases its functionality on the principle that almost all molecules absorb infrared (IR) light (λ>800nm). Only the monatomic (He, Ne, Ar, etc) and homopolar diatomic (H_2, N_2, O_2, etc) molecules do not absorb IR light. Molecules only

absorb IR light at those frequencies where the IR light affects the dipolar moment of the molecule. In a molecule, the differences of charges in the electronic fields of its atoms produce the dipolar moment of the molecule. Molecules with a dipolar moment allow infrared photons to interact with the molecule causing excitation to higher vibrational states. Only an oscillating dipole can absorb the IR light, provided that the frequency is matching. The intensity of the absorption (I) is proportional to the square of the change in dipole moment (μ) [11]:

where Q is the displacement coordinate of the motion.

$$I \propto \left[\frac{d\mu}{dQ}\right]^2 \qquad \{3.8\}$$

If a stretch does not change the dipole moment, there would not be any IR band. The FTIR spectrum is conventionally presented in the form of a graph of transmittance (T) or absorbance (A) against frequency (λ) or wave number (ν in cm^{-1})

$$T = \frac{I}{I_0}, A = \log\left[\frac{I_0}{I}\right] \qquad \{3.9\}$$

I_0 = Intensity of incident ray, I = Intensity of light at depth l in the medium.

Quantitative IR analysis is based on Beer-Lambert law which has been already discussed (in the section for UV-Visible spectroscopy).

A FTIR spectrometer is an instrument which acquires broadband near-IR (<650 cm^{-1}) to far-IR (>4000cm^{-1}) spectra. Unlike a dispersive instrument, i.e. grating monochromator or spectrograph, a FTIR spectrometer collects all wavelengths simultaneously.

FTIR spectrometer:

A FTIR is typically based on a Michelson Interferometer; for example as shown in Fig. 3.9.

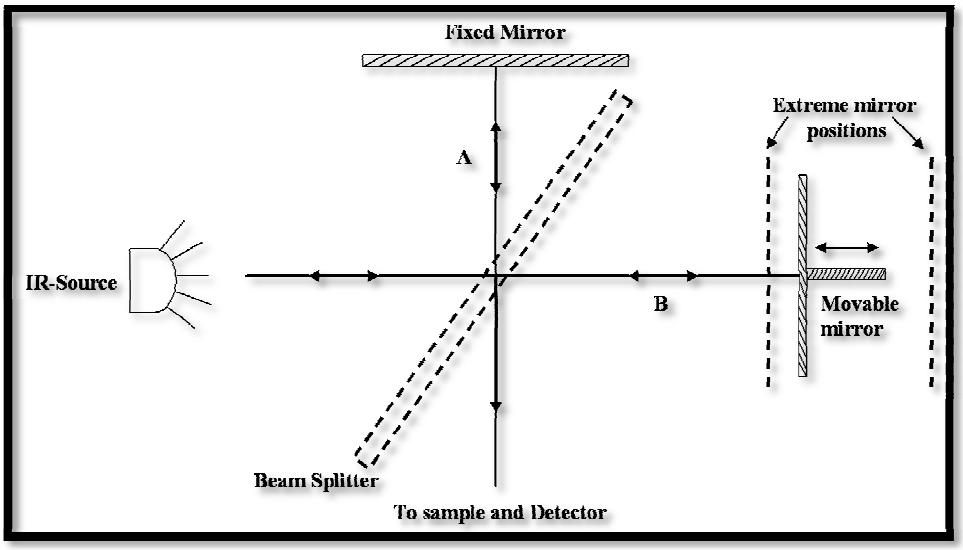

Figure 3.7: Schematic diagram showing layout of optical components in a Michelson interferometer.

The interferometer consists of a beam splitter, a fixed mirror, and a mirror that translates back and forth, very precisely. The beam splitter is made of a special material that transmits 50% of the radiation striking it and reflects the other half. Therefore, the interferometer splits a beam of radiation into two and then recombines the two beams after introducing a path difference.

The X-axis of the interferogram represents the optical path difference (OPD). Each individual spectral component contributes to this signal a single sinusoid with a frequency inversely proportional to its wavelength. Once an interferogram is collected, it needs to be translated into a spectrum (emission, absorption, transmission, etc.). The process of conversion is through the Fast Fourier Transform algorithm. This method was discovered by J.W. Cooley and J.W. Tukey in 1965.

Utility of FTIR Spectroscopy for Nanomaterials

IR spectroscopy has been extensively used to characterize organic compounds to detect functional groups with specific vibration frequencies [10]. Of late, researchers working in the field of nanosciences have started exploiting this technique to record the various vibrational frequencies in any nanomaterial.

To check the presence/absence of any specific chemical species and its coordination state in the nanomaterial, FTIR analysis is carried out in a narrow frequency interval, where the species of interest has a characteristic absorption [6]. The normal way to approach the interpretation of an IR spectrum is to examine the functional group region to determine which groups might be present, then to note any unusually strong bands or particularly prominent patterns in the fingerprint region. Multiplex advantage achieved with the FTIR measurement minimizes the adverse effects of environment on the highly-responsive surface of a nanomaterial. FTIR spectra with its superior resolution facilitate in capturing the vibrational modes arising from the various functional groups present in a nanomaterial.

Instrumental Details

All FTIR spectra were recorded with a single beam Perkin Elmer instrument (Spectrum BX-500) FT-IR Model spectrophotometer [Fig. 3.8]. This spectrometer allows us to collect spectra in mid-IR, far-IR and near-IR spectral ranges. The spectrum BX contains a CDRH Class II Helium Neon (HeNe) laser, which emits visible, continuous wave radiation at a wavelength of 633 nm nd has a maximum output power of less than 1mW. The recording abscissa range of this instrument is 400-4000 cm^{-1}. Each spectrum was collected with 64 scans co-added at 4 cm^{-1}resolution.

Figure 3.8: Perkin Elmer FTIR system

The normal operation mode of this spectrometer is temperature stabilized. The spectrometer utilizes continuous dynamic alignment to ensure exceptional high-resolution line

shapes. Its compact optical path minimizes beam path length and improves spectral performance by limiting the number of beam reflections, which translates into extremely reproducible results with no instrument drift. Before measurement the instrument is properly sealed and desiccated. The desiccant protects the beam splitter and other optical components by reducing the amount of water vapour inside the spectrometer.

Samples Used and Their Preparation

We have recorded the FTIR spectra for the FTIR spectra for the liquid samples in the transmission mode in the range of 400 – 4000cm^{-1}. For this purpose we have dissolved a known amount of the powdered nanomaterial in toluene as a solvent. The back ground is taken with the same solvent initially (generally toluene) and is subtracted automatically by the software, after acquiring the spectra.

3.2.5 Scanning Electron Microscopy

Scanning electron microscopy (SEM) is a powerful and popular technique for imaging the surfaces of almost any material with a resolution down to about 1 nm[6, 7]. The scanning electron microscope (SEM) uses a focused beam of high-energy electrons to generate a variety of signals at the surface of solid specimens. It utilizes the secondary electrons (SEs) and backscattered electrons (BSEs) being emitted from different areas of the specimen (as shown in figure 3.9) as well as the trajectories they take in relation to the location of the detector. The signals that derive from electron sample interactions reveal information about the sample including its size, shape, external morphology (texture), of the three dimensional samples. The SEM is also capable of performing analyses of selected point locations on the sample, this approach is especially useful in qualitatively or semi-quantitatively determining chemical compositions (using EDS), crystalline structure, and crystal orientations (using EBSD). The design and function of the SEM is very similar to the EPMA, and considerable overlap in capabilities exists between the two instruments.

The image resolution offered by SEM depends not only on the property of the electron probe, but also on the interaction of the electron probe with the specimen. Interaction of an incident electron beam with the specimen produces secondary electrons, with energies typically smaller than 50

eV, the emission efficiency of which sensitively depends on surface geometry, surface chemical characteristics and bulk chemical composition. The SEM has a large depth of field, which allows a large amount of the sample to be in focus at one time and produces an image that is a good representation of the three-dimensional sample.

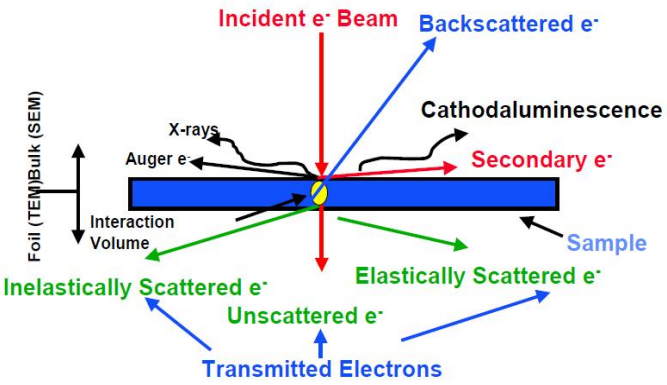

Figure 3.9: Interaction of high energy electrons with solid.

The combination of higher magnification, larger depth of field, greater resolution, compositional and crystallographic information makes the SEM one of the most heavily used instruments in academic/national lab research areas and industry.

Figure 3.10: Zeiss EVO MA-10 variable pressure SEM.

The $CuInSe_2$ nanoparticles were imaged using scanning electron microscopy (SEM, Zeiss EVO MA-10 variable pressure SEM, figure 3.10) of resolution 3nm with probe current of 100 picoamp. It works in SEI mode i.e. it utilizes secondary electrons emitted from sample surface. Samples are scanned at accelerating voltage of 10.00 KV and WD of 12.00 mm at different magnifications from 1.00 KX - 30.00 KX under vacuum pressure of 10^{-6} torr.

3.2.6 Transmission Electron Microscopy

The transmission electron microscopy is a powerful technique to study the microstructure of the sample. Using this technique grain size and shape, orientation of the grains, crystalline defects, lattice images, etc. can be investigated.

Theory

The basic principle of lattice imaging by TEM is discussed in the following subsections.

Direct Lattice Resolution

In this case two coherent beams, i.e., one undeviated and one diffracted beam reach the image plane after passing through the same point of the sample, and a periodic variation in the intensity is observed. This periodicity “d” is equal to the spacing between the planes of the atoms. Since the angle of the deviation for a diffraction beam is inversely proportional to the interplaner spacing, the smallest spacing requires the use of larger objective apertures.

Even a small amount of contamination on the edge of the aperture can cause sufficient electrostatic charging and lead to a serious distortions of a beam passing close to its edge, and hence a loss of resolution. It us not worthwhile increasing the size of the objective aperture beyond a certain point, to allow higher angle diffracted beam to be used to form images, because the higher order beam results in sufficiently large aberrations to prevent the periodic structure in the image from being resolved. The use of more than one diffracted beam is an advantage when beams diffracted by more than one set of crystal planes, are included. Provided the spacing between these different planes are within the resolution limit of the microscope, this allows a

two-dimensional, lattice image of a crystal to be formed. In this way all the periodicities perpendicular to the electron beam, are revealed on one image.

Indirect Lattice Resolution

The periodic structure of a crystal can be revealed by means of moiré patterns from overlapping crystals, even when the actual periodicities are below the resolution limits of the microscope. We therefore call this as the indirect lattice resolution.

If two overlapping gratings are parallel, but differ in spacings, so producing a structure with a double periodicity. Beats are formed between these two periodicities, with a spacing D given by,

$$D = \frac{d_1 d_2}{d_1 - d_2} \qquad \{3.10\}$$

Where, d_1 and d_2 are the lattice spacings of the overlapping first and second crystals respectively.

In rotation moiré pattern the two gratings have identical spacings d but are rotated with respect to each other by a small angle. In this case the spacing D is given by,

$$D = \frac{d}{2Sin(\alpha / 2)} \qquad \{3.11\}$$

Instrumental Details

A transmission electron microscope (REM), JEOL make model JEM-200CX has been used to study the microstructure of the colloidal nanoparticles. The photograph of the TEM is shown in the Fig. 3.11. It has a resolution of 3.5Á (point to point) and 1.44 Á (lattice). The magnification of the instrument could be varied form 100X to 4,50,000X while the accelerating voltage could be varied from 80, 100, 120,160 and 200 kV. Selected area diffraction pictures could be taken with the diffraction camera length varying from 160mm to 240mm. It is a fully automated vacuum system. The state of art electronics circuits, logical and compact design facilitates both operation and maintenance. For example, start up, shut down and photography can be executed by a simple push button operation. Magnification and camera length can be directly read out regardless of any change in the accelerating voltage and recorded together with the film number on the film. Moreover the microscope provides very stable and excellent images at low to high magnification and a variety of diffraction patterns instantly. The available attachments can

permit the specimen to be heated cooled, tilted in-situ and also enable various signals from the specimen to be observed.

The column of the microscope consists of an electron gun, two stage condenser lens, and interlocking two stage beam reflector, specimen chamber, the image forming system which is normally composed of an objective lens, two stage intermediate lens and a projector lens. Viewing chamber and camera chamber are also the parts of the column. The specimen chamber has a side entry stage. The specimen exchange device contains an air lock mechanism so that the specimen can be exchanged without breaking the column vacuum. The specimen holder has a capacity of holding two specimens. The specimen movement range in X and Y directions are ±1mm while along the Z direction it is ± 0.5 mm. The specimen can be tilted by an angle of ± 30^{o} C (X tilt). The viewing chamber consists of a viewing window to see image of the specimen formed on the fluorescent screen. A binocular with a clear field is also installed with it to see the ten times enlarged for image focusing purposes. The approximate size of an individual particle in the image of the specimen on a photographic screen can also be estimated with the help of small scale provided on the photographic screen.

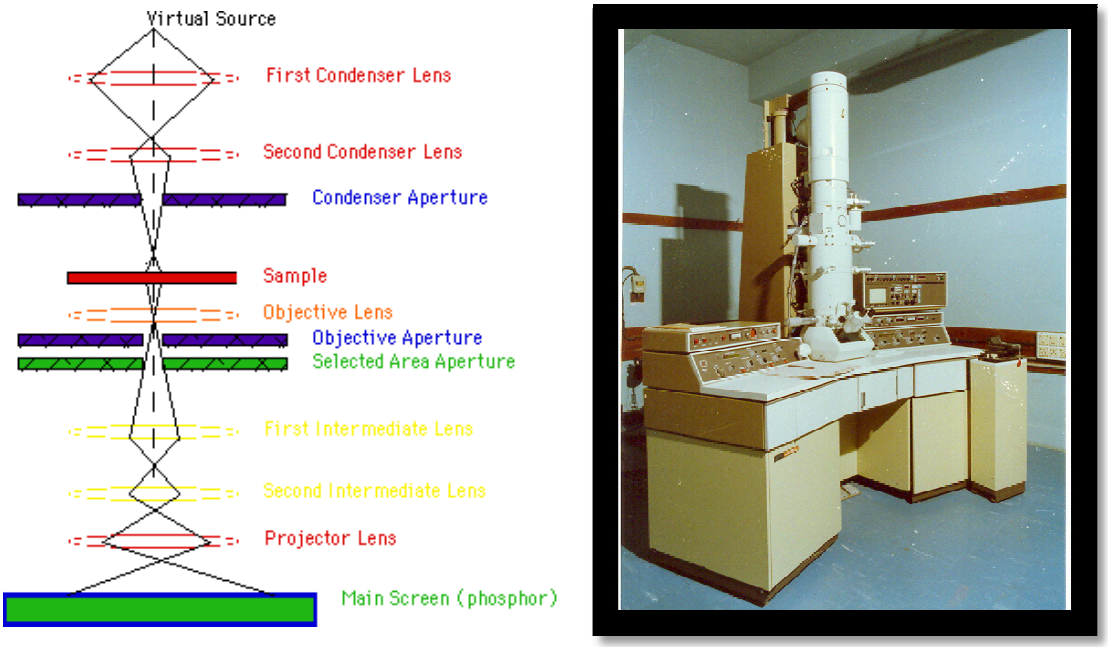

Figure 3.11: Transmission Electron Microscope

This instrument has a fully automatic camera complete with a data recording device and its specially designed automatic exposure mechanism ensures optimum exposure. Since this camera is equipped with an air lock mechanism, rapid film exchange can be executed without breaking the vacuum of the column. The camera chamber has films loading capacity up to 50. The cut film having a size 65mm X 90 mm, supplied by Eastman Kodak company USA were used for recording purpose.

Samples Used and Their Preparation

For viewing the morphology of the nanoparticles formed, aliquots of CdSe nanoparticles were washed several times in methanol to remove the extra TOPO groups. Very dilute solutions of these washed nanoparticles in methanol were dropped on carbon coated meshed TEM grids and the solvent was allowed to evaporate leaving the nanoparticles on the grid. These grids were then loaded in the vacuum chamber of the microscope for viewing.

3.2.7 Atomic Force Microscopy(AFM)

Atomic Force Microscopy (AFM) is a form of scanning probe microscopy (SPM) where a small probe is scanned across the sample to obtain information about the sample's surface .

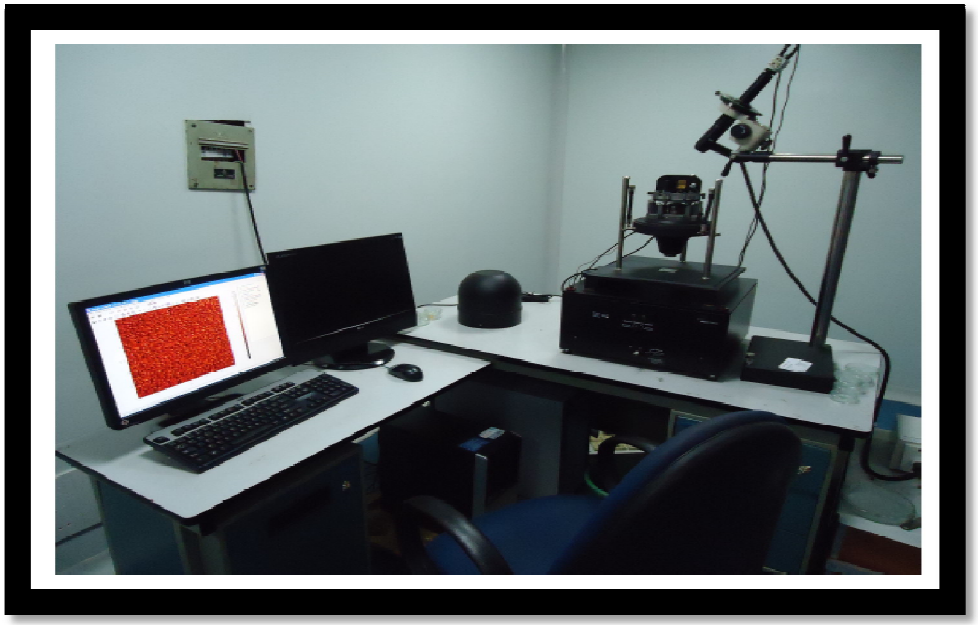

FIGURE 3.12 AFM set up

. The information gathered from the probes interaction with the surface could be as simple as physical topography or as diverse as measurements of the material's physical, magnetic, or chemical properties. These data are collected as the probe is scanned in a raster pattern across the sample to form a map of the measured property relative to the X-Y position. Thus, the AFM microscopic image shows the variation in the measured property, e.g., height or magnetic domains, over the area imaged.

The AFM probe has a very sharp tip, often less than 100Å diameter, at the end of a small cantilever beam. The cantilever is typically silicon or silicon nitride with a tip radius of curvature on the order of nanometers. When the tip is brought into proximity of a sample surface, forces between the tip and the sample lead to a deflection of the cantilever according to Hooke's law.

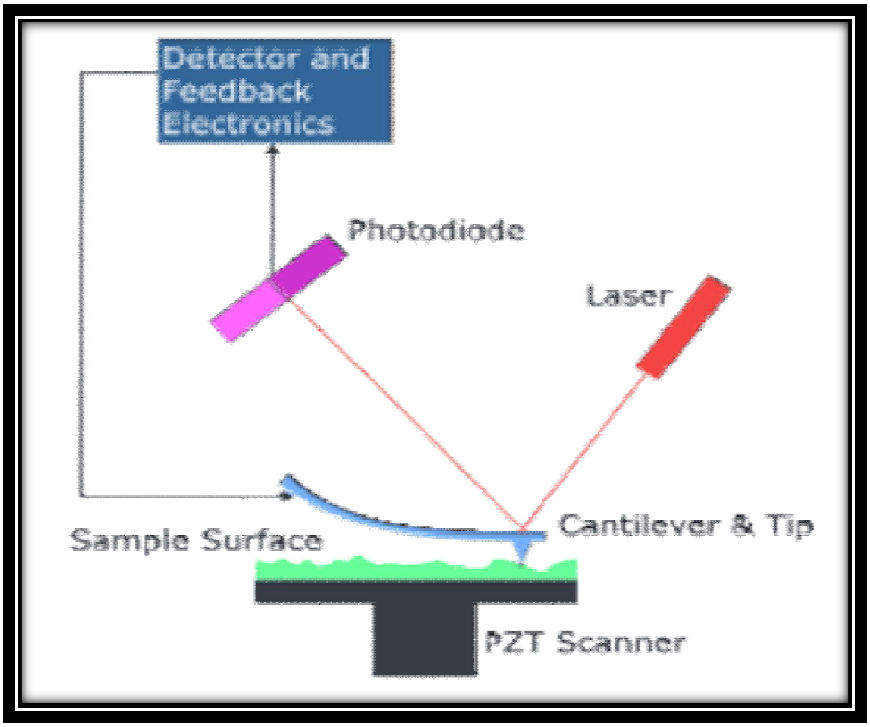

Fig 3.13 Block diagram of atomic force microscope

Typically, the deflection is measured using a laser spot reflected from the top surface of the cantilever into an array of photodiodes as shown in Figure above. Using a Wheatstone bridge, strain in the AFM cantilever due to deflection can be measured, but this method is not as sensitive as laser deflection or interferometry.

If the tip was scanned at a constant height, a risk would exist that the tip collides with the surface, causing damage. Hence, in most cases a feedback mechanism is employed to adjust the tip-to-sample distance to maintain a constant force between the tip and the sample. Traditionally, the sample is mounted on a piezoelectric tube that can move the sample in the z direction for maintaining a constant force, and the x and y directions for scanning the sample. Alternatively a 'tripod' configuration of three piezo crystals may be employed, with each responsible for scanning in the x,y and z directions. This eliminates some of the distortion effects seen with a tube scanner. The resulting map of the area s = f(x,y) represents the topography of the sample. Areas as large as about 100 μm squares to less than 100 nm square can be imaged. The AFM can be operated in a number of modes, depending on the application. In general, possible imaging modes are divided into:

Contact Mode AFM - The AFM probe is scanned at a constant force between the probe and the sample surface to obtain a 3D topographical map. When the probe cantilever is deflected by topographical changes, the scanner adjusts the probe position to restore the original cantilever deflection. The scanner position information is used to create a topographical image. Lateral resolution of <1 nm and height resolution of <1 Å can be obtained.

Intermittent Contact (Tapping Mode) AFM - In this mode, the probe cantilever is oscillated at or near its resonant frequency. The oscillating probe tip is then scanned at a height where it barely touches or “taps” the sample surface. The system monitors the probe position and vibrational amplitude to obtain topographical and other property information. Accurate topographical information can be obtained even for very fragile surfaces. Optimum resolution is about 50 Å lateral and <1 Å height. Images for phase detection mode, magnetic domains, and local electric fields are also obtained in this mode.

Image Analysis - Since the images are collected in digital format, a wide variety of image manipulations are available for AFM data. Quantitative topographical information, such as lateral spacing, step height, and surface roughness are readily obtained.

Typical applications

3-dimensional topography of IC device, roughness measurements for chemical mechanical polishing,analysis of microscopic phase distribution in polymers, mechanical and physical property measurements for thin films, imaging magnetic domains on digital storage media, imaging of submicron phases in metals, defect imaging in ic failure analysis, microscopic imaging of fragile biological samples,and metrology for compact disk stampers.

Atomic force microscope (AFM) measurements were done in tapping mode. AFM pictures were applied to check the roughness of the films: this was used to see the distribution of the materials in bulk heterojunction cells, to estimate the size of the zinc sulfide nano-particles and to see if the material makes a real film or if there are just islands of the material within the device.

References

1. .W.W. Yu, J.C. Falkner, B.S. Shih, V.L. Colvin, Chem. Mater. 16, 3318(2004)
2. Q. Dai, Y. Wang, X. Li, Y. Zhang, D.J. Pellegrino. ACS Nano. 3, 1518 (2009)
3. Jeffrey M. Pietryga, Donald J. Werder, J. AM. CHEM. SOC. 2008, 130, 4879-4885 9 4879
4. B. D. Cullity, Elements of X-Ray Diffraction, Addition-Wesley Publishing Company Inc. U.S.A.
5. L. V. Azaroff, Elements of X-Ray Crystallography, McGraw-Hill, U.S.A. (1968).
6. W. Kemp, Organic Spectroscopy, ELBS and Macmillan Press Ltd.
7. S. V. Gaponenko, Optical Properties of Semiconductor Nanocrystals, Cambridge University Press (1998).
8. J. I. Pankove, Optical Processes in Semiconductors, Dover Publications, Inc., New York (1971).
9. C. P. Poole, Jr. and F. J. Owens, Introduction to Nanotechnology, Wiley-Interscience, U.S.A. (2003).
10. H. A. Szymanski and R. E. Erickson, Infrared Band Handbook-volume 1,IFI/Plenum, New York
11. U. W. Gedde, Polymer Physics, 1st edition, Chapman & Hall, London (1995).

Properties of Single Pot Synthesized Composition Tunable PbSe-CdSe Core-Shell and $Cd_XPb_{1-X}Se$ Nanocrystallites

CHAPTER - 4

Phase-I (Synthesis)

4.1 Synthesis of PbSe-Core Nanostructures

Monodispersed PbSe-core nanostructures are synthesized by chemical method described by Murray et al [1]. For a typical synthesis of Oleic Acid/TOP-capped PbSe-core nanocrystals, 1.5 g of lead acetate and 5.1 ml of Oleic acid were dissolved in 25ml phenyl ether, the reaction mixture was heated to 140 °C for 1hr under stirring and under continuous flow of argon and then cooled .when the temperature of the phenyl ether solution fell below 70 °C,12 ml of 1M TOPSe was added for the formation of molecular precursor solution. The injection and growth temperature was varied from 80 °C to 150 °C to obtain the desired particle size. Higher growth temperatures were used to prepare larger sized PbSe-core nanostructures. After injection the reaction mixture was maintained at the growth temperature for 5-10 minutes and then colloid was cooled to approximately 0 °C and stored in hexane after thoroughly washed with the desired reagents as methanol in this case.

Required Chemicals:

Lead Oxide (99.99%), Oleic Acid (90%), Selenium (99.5%), Trioctylphosphine (90%),Diphenyl ether (99%),Methanol and Hexane.

4.2 Synthesis of PbSe-CdSe core-shell structure

The chemical required for the synthesis of core shell material is same as used in the preparation of PbSe-core nanoparticles. Cadmium Oxide (99.99%) was also used for shell formation. PbSe-CdSe core-shell nanostructures were synthesized using novel single pot synthesis method. Here cadmium oxide was used as a cadmium precursor and its amount was varied (from 0 to 20%) as per the molarity ratio of CdSe/PbSe. Experimentally, cadmium precursor, lead precursor, oleic acid and phenyl ether were heated in a round bottom flask up to 140 °C in Ar atmosphere for 1hr under constant stirring. The mixture was then cooled down to 70 °C and solution of TOPSe as prepared in above method was added drop wise. The temperature was maintained growth temperature for few minutes before the mixture was cooled to room temperature to obtain the product.

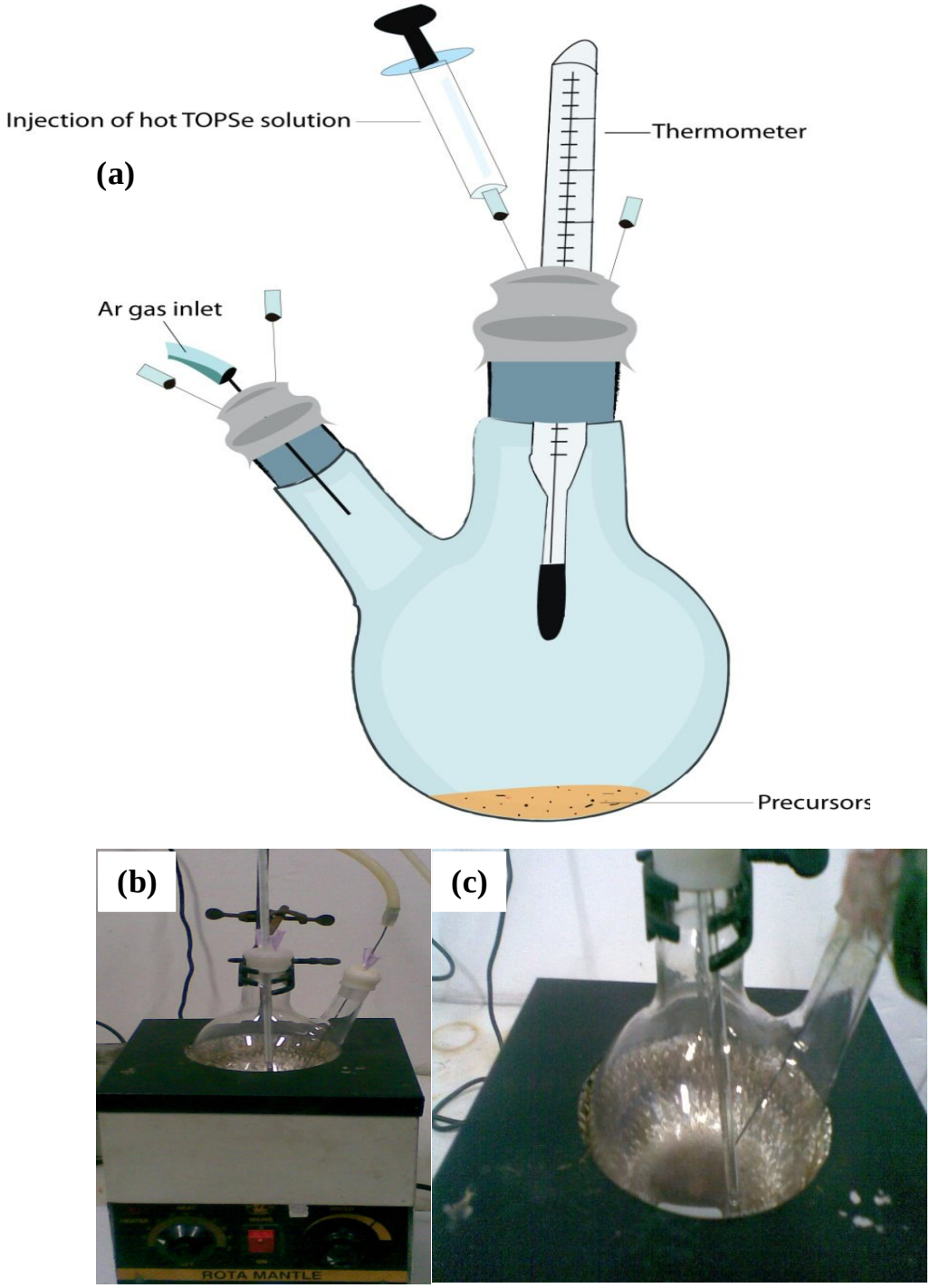

Figure 4.1 (a) Schematic of the apparatus used for synthesizing PbSe-core and PbSe-CdSe core-shell and $Cd_XPb_{1-X}Se$ nanocrystallites. (b) & (c) real images of synthesis setup at the time of experiment.

Phase-II (Characterization)

4.3 FTIR (Fourier Transform Infra Red) Spectrum

Fig4.2 (a)-(f) shows FTIR spectra of pure Oleic acid, Oleic acid capped PbSe-core nanocrystals,

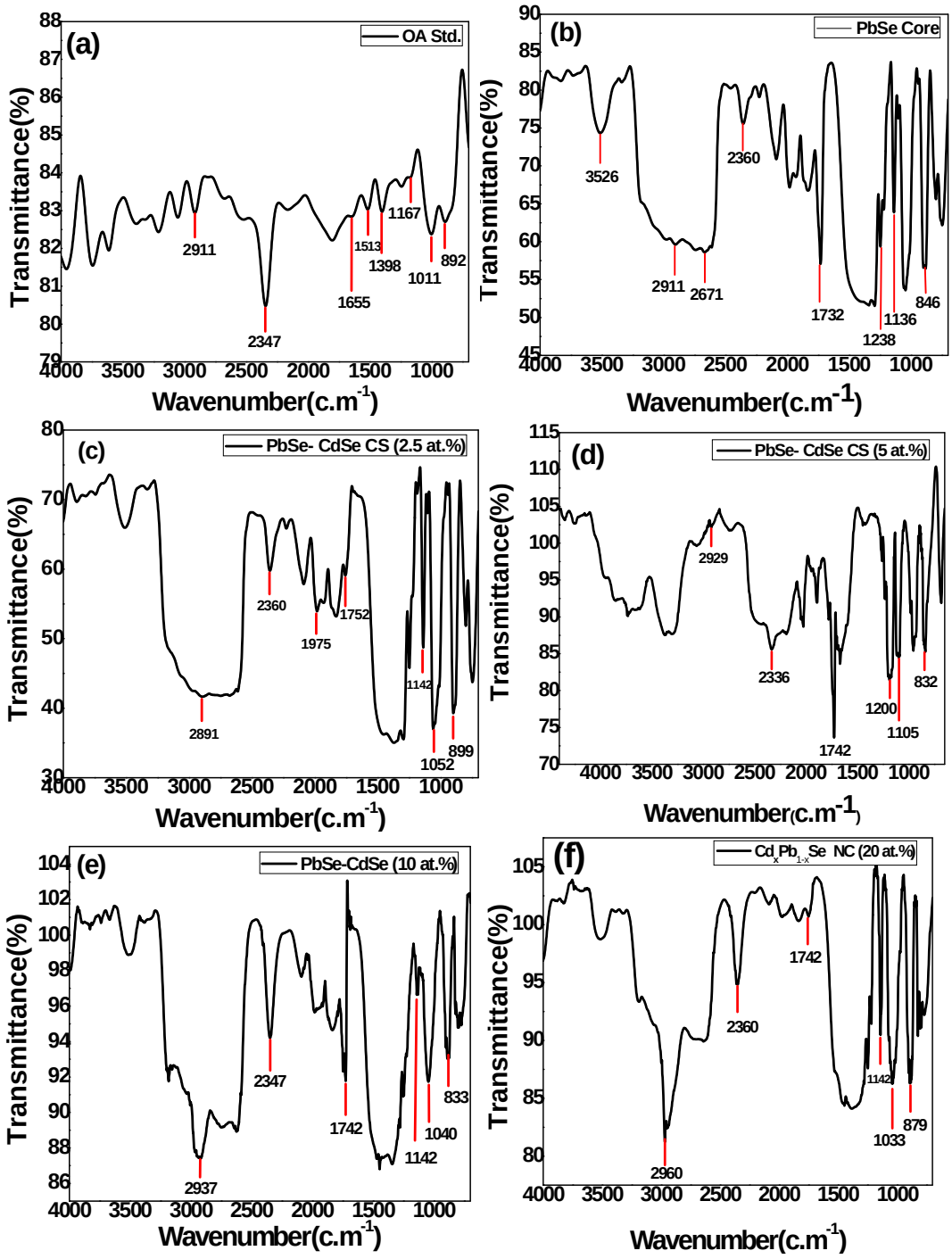

Figure 4.2. FTIR spectra of (a) oleic acid(b) PbSe-core(c)PbSe-CdSe core-shell(2.5 at.%),(d) PbSe-CdSe core-shell (5at.%)(e) PbSe-CdSe (10 at.%) & (f) $Cd_XPb_{1-X}Se$ nanocrystallites(NC) (20at.%).

PbSe- CdSe core- shell structures (2.5 at.%, 5at.%), PbSe-CdSe (10 at.%) and Cd_x $Pb_{1-x}Se$ nanocrystallites (20 at.%) respectively.

In pure Oleic acid, the characteristic peak in the band (1650-1742) $c.m^{-1}$ is the characteristic stretching vibration of C=O in carboxylic acid (COOH) and peak at 2911 $c.m^{-1}$ is attributed to the asymmetric CH2 stretching. The peaks in band 2880-2990 shows the existence of =C-H group and long alkyl chain in the oleic acid. IR peaks in band 1100- 1200 cm^{-1} shows the presence of P=O stretching mode corresponding to phosphine oxide in tri octyl phosphine (TOP) [2*]. It is clear from fig.1 (a)-(f), the characteristic peak of C=O in COOH group and peak for P=O in TOP, are present in band 1730-1752 and 1100-1200 $c.m^{-1}$ for all samples respectively. It shows the efficient capping of oleic acid and TOP ligand on surface of lead selenide nanostructures and gives the evidence that they are strongly intact to passivate the surface of nanocrystals.

4.4 Structural Properties

4.4.1 X-Ray Diffraction Analysis

X-ray diffraction was performed at room temperature on a Rigaku Miniflex-II with Cu Kα radiation. Table 4.1 shows the reference data of CdSe and PbSe crystalline phase.

Crystalline phase	**2 theta (reference)**	**Crystalline phase**	**2 theta (reference)**
PbSe	**25.16 (111)** **29.12 (200)** **41.66 (220)** **49.35 (311)** **51.62 (222)** **60.38 (400)** **66.44 (331)** **68.41 (420)** **76.04 (422)**	**CdSe**	**23·88 (100)** **25.20 (111)** **25·39 (002)** **27·09 (101)** **41·99 (110)** **42.10 (220)** **45·81 (103)** **49·72 (112)** **49.90 (311)**

Table 4.1 X-ray diffraction reference data for PbSe and CdSe [2],[3]

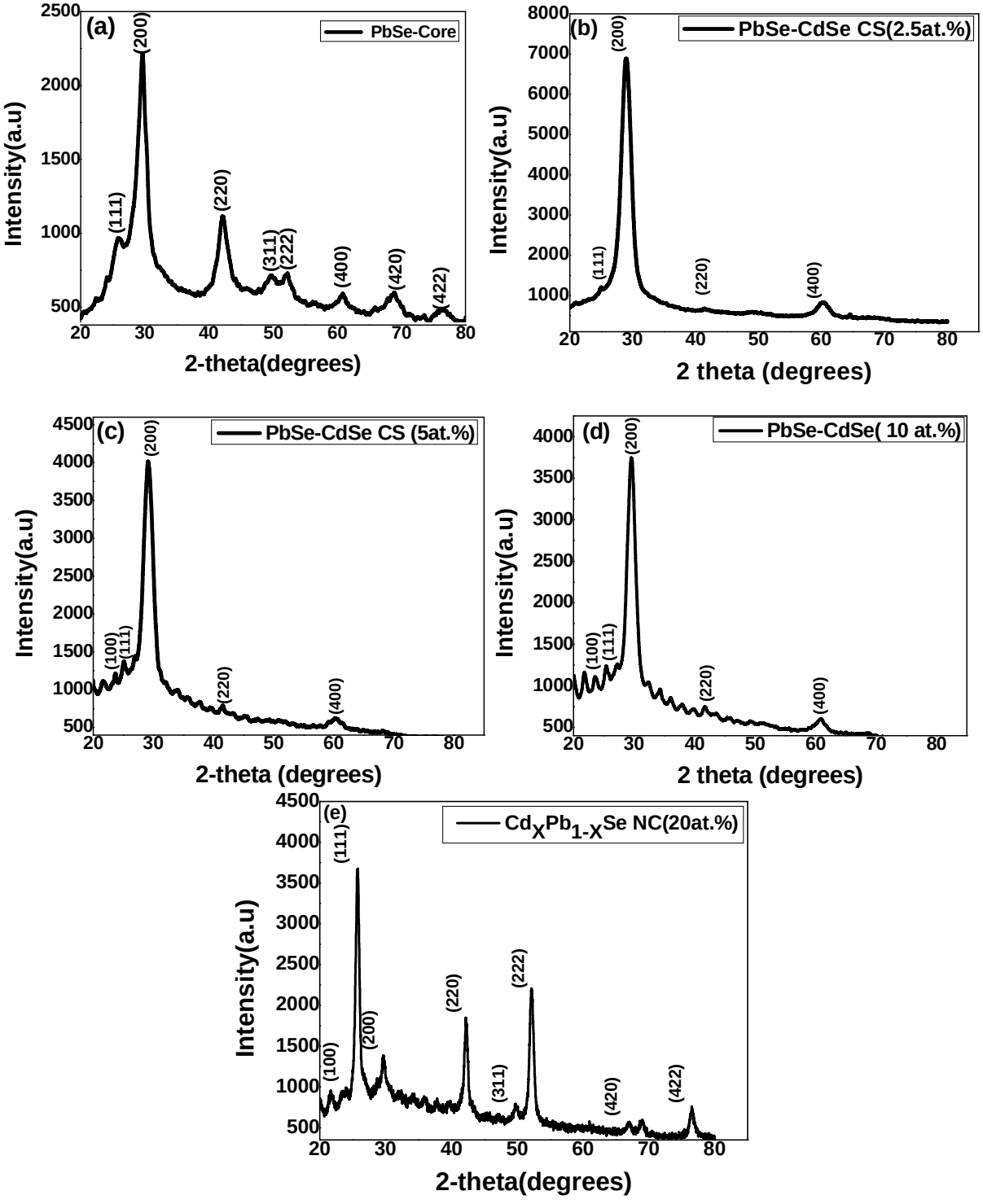

Figure 4.3 XRD pattern of (a) PbSe-core (b)PbSe-CdSe core-shell(2.5 at.%),(c) PbSe-CdSe core-shell (5at.%)(d) PbSe-CdSe (10 at.%) & (e) $Cd_XPb_{1-X}Se$ nanocrystallites (NC) (20at.%).

In figure 4.3 (a) The XRD patterns of PbSe nanoparticles show all possible peaks for PbSe crystals within the observed range of angles. Since all "h,k, l" values were all even or all odd, one can confirm that the PbSe nanocrystals have a perfect rock-salt (FCC) structure. The X-ray diffraction in exhibits clear peaks that confirm the rock salt crystal structure and are in well agreement with the simulated pattern, which is carried out using the data in JCPDS card File No.06-0354[4] and matched with the data given in table 4.1.In PbSe rock salt structure, the principal peak (200) is ,followed by (222) and then (111) respectively[3].The peak broadening justifies the PbSe core nanostructures formation. Also, the crystallite size as calculated by Scherrer's formula (as given in last chapter) is 26.49 nm which in 1-100nm range.

Also from X-ray diffraction pattern one can determine the "lattice parameter" of PbSe nanocrystals. It can be calculated by using following equation.

$$a = \frac{\lambda\sqrt{h^2 + k^2 + l^2}}{2\sin(\theta)} \qquad (4.1)$$

Where λ=1.5406 Å and h,k.l are corresponding miller indices for each angle.Table 4.2 shows the calculated values for lattice parameter for each XRD peak.

Angle (2□)	h, k, l	Lattice parameter (Å)
25.49	111	6.040
29.56	200	6.039
42.20	220	6.053

Table 4.2: Miller indexes and Lattice parameters of PbSe nanocystals calculated from XRD peaks obtained from Fig. 4.1.

According to the table, the lattice parameter for PbSe nanocrystals was found to be 6.044 A^o. The calculated values of lattice parameters are in well agreement with the cubic (rock salt) bulk PbSe lattice parameter of 6.128A^o.

In figure 4.3(b) The XRD pattern of PbSe-CdSe core-shell structure having Cd~ 2.5at.% shows that the principal peaks in PbSe a rock salt lattice (200), (111) and (220) are present in this pattern(compared with fig.4.3(a)). The intensity of the highest peak increases as well as the planes which were present in the PbSe core structure were suppressed due to the presence of shell (CdSe) over the core (PbSe) while the intensity of 111 peak increased as, in CdSe, a zinc-blende lattice, the 200 is essentially absent, the 111 is the principal peak, and the 220 remains substantial [3]. The crystallite size as calculated using Scherer's formula is 26.49 nm. Figure 4.3(c) The XRD pattern of PbSe-CdSe core-shell structure having Cd~5at.% shows that the principal peak of PbSe-core structure is present with higher intensity than PbSe core structure. Due to more concentration of CdSe, peak (111) become more intense as compare to the core sample as it is principal peak in CdSe bulk.[3], 200 is present having less intensity. The combine effect is observed in this pattern which confirms the presence of CdSe shell on the PbSe-core. The crystallite size as calculated using Scherer's formula is 26.49 nm. Figure 4.3(d) shows the XRD pattern of PbSe-CdSe nanostructure having Cd~10at.% shows that with increase in concentration of Cd precursor the peak that are present in CdSe structure are also show their effect as 100 peak at angle 23.80 is present in CdSe bulk structure also have contribution in this pattern residing before 111 peak. In Figure 4.3(e) shows the XRD pattern of ternary $Cd_XPb_{1-X}Se$ nanocrystallites having Cd~20at. % depicts different behavior as the peaks which are absent in PbSe-core sample are clearly visible in this XRD pattern. The 111 peak become highly intense in this case as principal peak (200)in PbSe is now suppressed due to the formation of alloy rather than core-shell. From the XRD analysis it is confirmed as we are increasing the concentration of CdO precursor, their presence is clearly visualize from the diffraction pattern at higher concentration.

4.3.2 Study of Morphology of Nanocrystallites

4.3.2.1 TEM Micrographs

1n figure 4.4 (a)The TEM image of PbSe-core nanostructure shows that quantum dots has been successfully prepared having the average diameter of 7 nm as determined from the images. The image also shows the particles are spherical in shape and size distribution to be relatively narrow. Figure 4.4(b) the TEM image of PbSe-CdSe core shell structure having Cd~2.5at.%, depicts the enhanced contrast between the CdSe (outer shell, darker in color) and

PbSe (lighter ,inner core) reveals the anticipated core/shell structure[3],the inset show the magnified image of the structure. These images confirm the formation of core shell structure. The particle diameter as calculated through the image is 8 nm.The particles formed within the nanometer range 1-100 nm. Figure 4.4(c) is TEM image of PbSe-CdSe core shell structure having Cd~5at.%, shows that the outer region is thick as compared to the previous core shell structure. The outer region is dark while the inner region is bright. The particle size as calculated is ~ 10 nm. Encircle region clearly shows the formation of core-shell nanostructures. Figure 4.4 (d) is the TEM image of PbSe-CdSe nanostructure having Cd~10at. % shows the presence of both species showing different contrast in image and uniformly distributed. Figure 4.2(e) shows the TEM image of ternary $Cd_XPb_{1-X}Se$ nanocrystallites having Cd~20at.% which depicts the particles are uniformly distributed having two different types of particles but they don't have spherical shape, due to which particle size cannot be calculated.

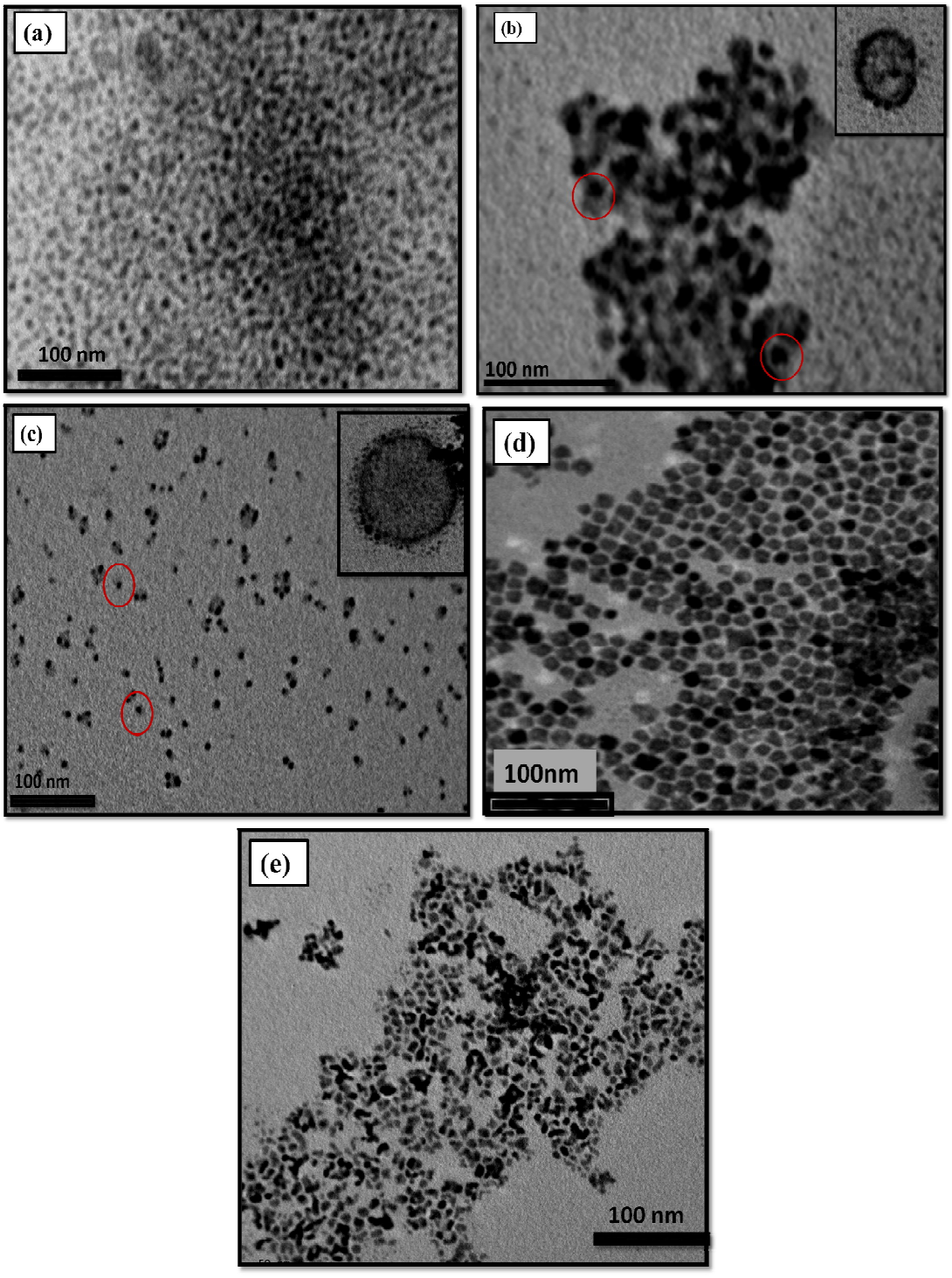

Figure 4.4 TEM images of (a) PbSe-core(b)PbSe-CdSe core-shell(2.5 at.%),(c) PbSe-CdSe core-shell (5at.%)(d) PbSe-CdSe (10 at.%) & (e) $Cd_XPb_{1-X}Se$ nanocrystallites(NC)(20at.%).

4.3.2.2 SEM Micrographs

SEM images in figure 4.5 (a) shows the surface morphology of PbSe-Core nanostructures .The shape of particles seems to be spherical figure 4.5.(b)shows the of image of PbSe-CdSe core-shell structure having Cd~2.5at.%. SEM images clearly shows that inner part is dark while the outer part is bright that confirm the presence of two different materials. SEM image 4.5(c) shows the PbSe-CdSe core -shell structure having Cd~5at.%, and thick shell formation over the core this is due to increase amount of CdO precursor. The shell is relatively thick than the previous case of PbSe-CdSe core-shell. Figure 4.5(d) shows co-existence of both core-shell and alloy nanostructures in PbSe-CdSe nanostructure having Cd~10at. % . It shows that the particle get agglomerated and due to more concentration of precursor we get more brighter region which shows higher concentration of Cd precursor as compare to the PbSe-CdSe core-shell. It shows the reduction in number density core-shell nanocrystallites and concurrent increment in alloy nanostructures. In fig. 4.5(e) ternary $Cd_XPb_{1-X}Se$ nanocrystallites having Cd~20at. %, image shows the formation of alloy as it is clear from figure that dark region is maximum surrounded by bright region but not typical shell structure which confirms that as we are increasing the atomic percentage of CdO precursor the typical shell formation transform to the alloy form, as it is also confirms from the XRD phase information where CdSe peaks are dominant on PbSe phases and reduce the peak intensity. So SEM results are in well agreement with TEM and XRD information, which gives the morphological as well as phase information.

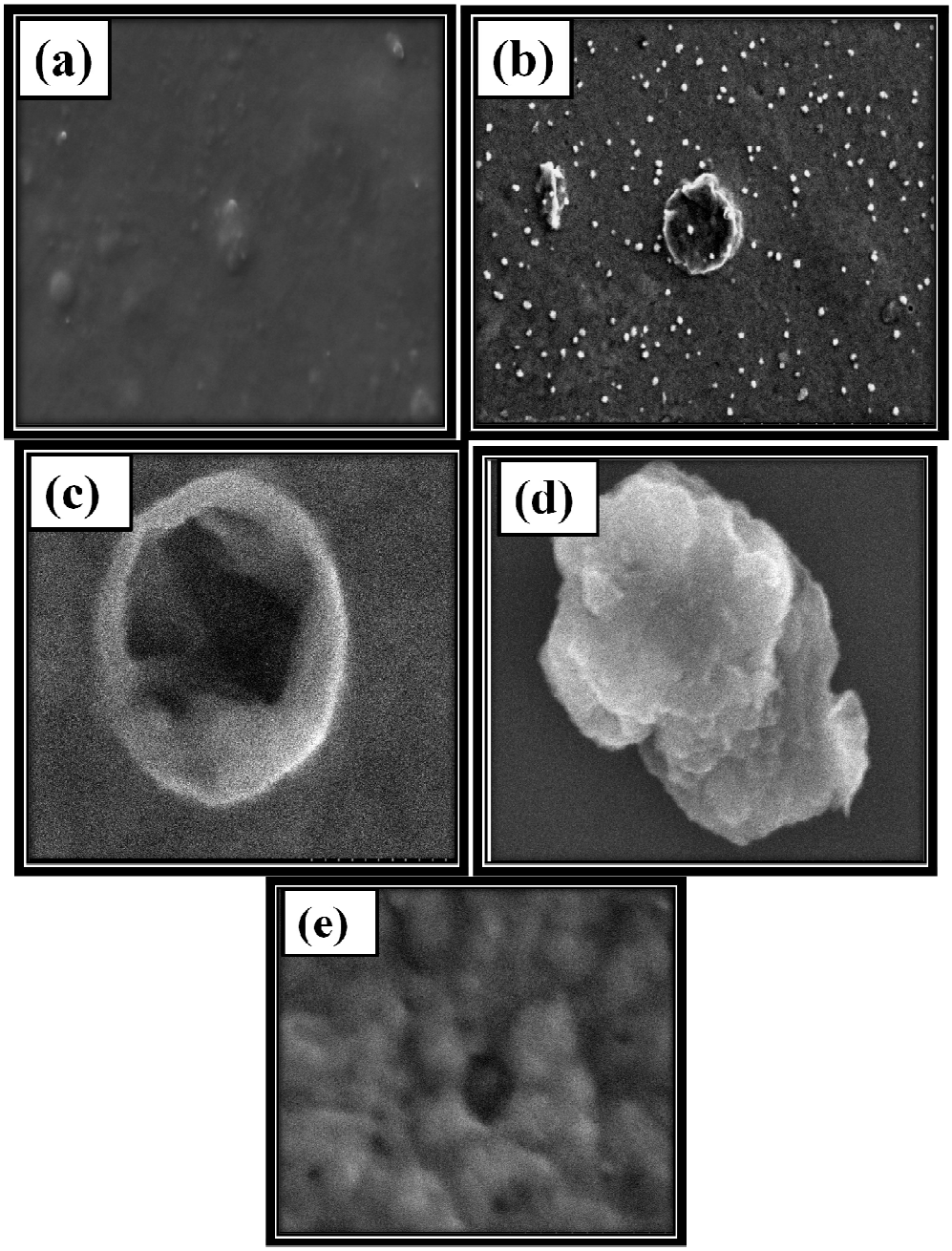

Figure 4.5. SEM images of (a) PbSe-core(b)PbSe-CdSe core-shell(2.5 at.%),(c) PbSe-CdSe core-shell (5at.%)(d) PbSe-CdSe (10 at.%) & (e) $Cd_XPb_{1-X}Se$ nanocrystallites(NC)(20at.%).

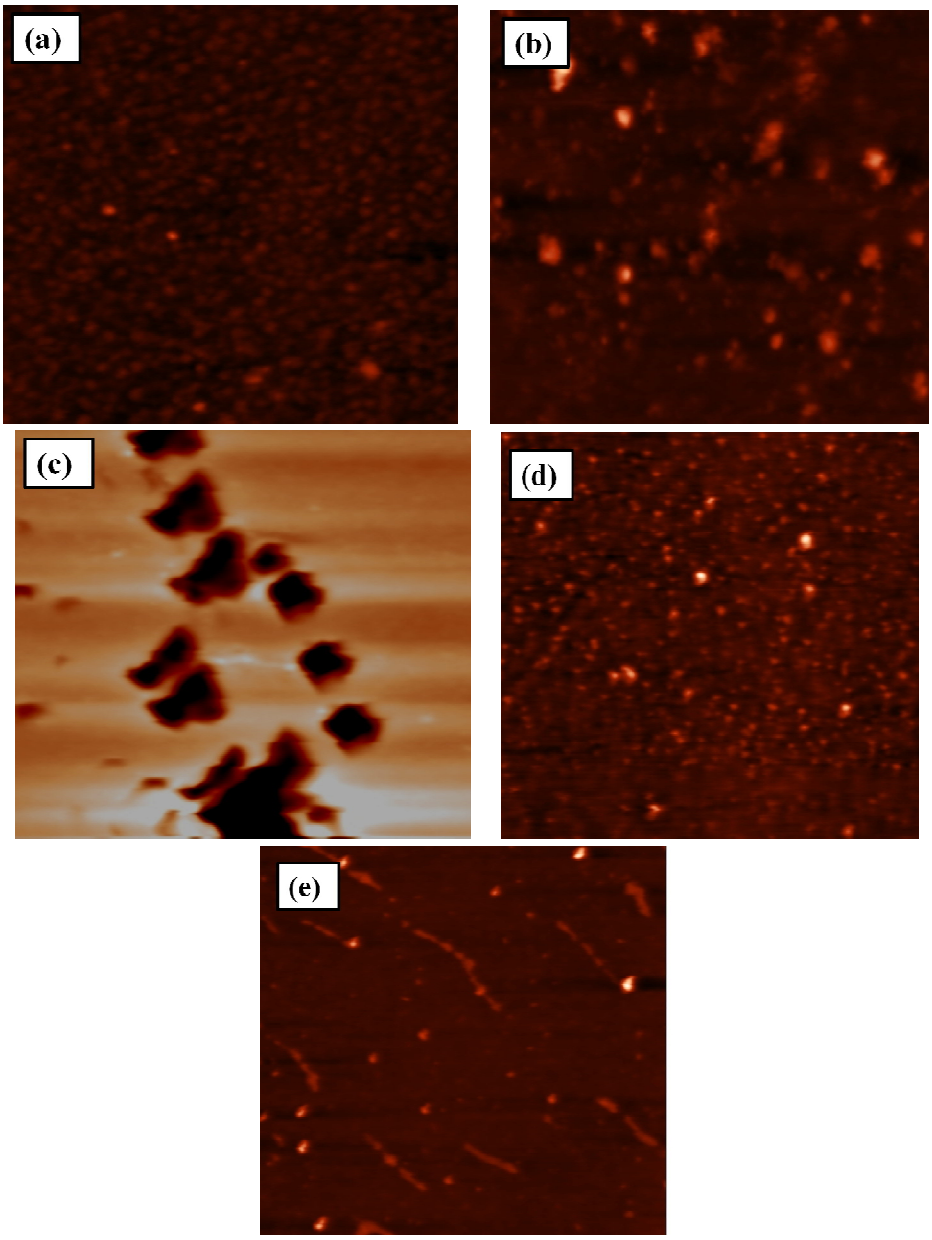

Figure 4.6. AFM images of (a) PbSe-core(b)PbSe-CdSe core-shell(2.5 at.%),(c) PbSe-CdSe core-shell (5at.%)(d) PbSe-CdSe (10 at.%) & (e) $Cd_XPb_{1-X}Se$ nanocrystallites (NC)(20at.%).

Figure 4.6 shows the image of (a) PbSe-core shows the uniform distribution of particles and the images were taken using semi-contact mode. Figure 4.6 (b) and (c) shows the image of PbSe-CdSe core-shell(2.5 at.%) and PbSe-CdSe core-shell (5at.%) respectively. It is clear from the fig (b) and (c) that particle size is increased as we are increasing the atomic percentage of Cadmium precursor which gives the evidence of shell formation on PbSe core due to which size is increased as clearly seen from the images whereas fig. 4.6 (d) shows uniform distribution of particles in PbSe-CdSe (10 at.%) as well as presence of two different species can be clearly seen with different contrast in image. Figure 4.6 (e) $Cd_XPb_{1-X}Se$ nanocrystallites (NC)(20at.%) shows the presence of two different material more clearly as it has maximum amount of Cd precursor as compare to the other structures, which also reflects two types of formations but not in spherical shape. So the results obtained by AFM are in well agreement with SEM and TEM micrograph information.

4.3.3 Optical Characterization

The visible- IR absorption spectra of nanocrystalline PbSe shows absorption edge at λ=1768.22nm.The band gap can be calculated using relation

$$E_g = \frac{1240.59}{\lambda(nm)} \text{ (eV)} \qquad (4.2)$$

Band gap of the PbSe nanocrystals is 0.702 eV as computed by extrapolation of the absorption edge. The band gap values as calculated above absorption edge confirm the quantum confinement of these PbSe-core semiconductor nanocrystals. In bulk PbSe semiconductor the band gap is 0.28eV. As the size of the semiconductor NC decreases, bangap is increasing which is the direct evidence of nanoparticles formation. that absorption peaks shifted towards high energy, thus confirming the strong confinement effects.

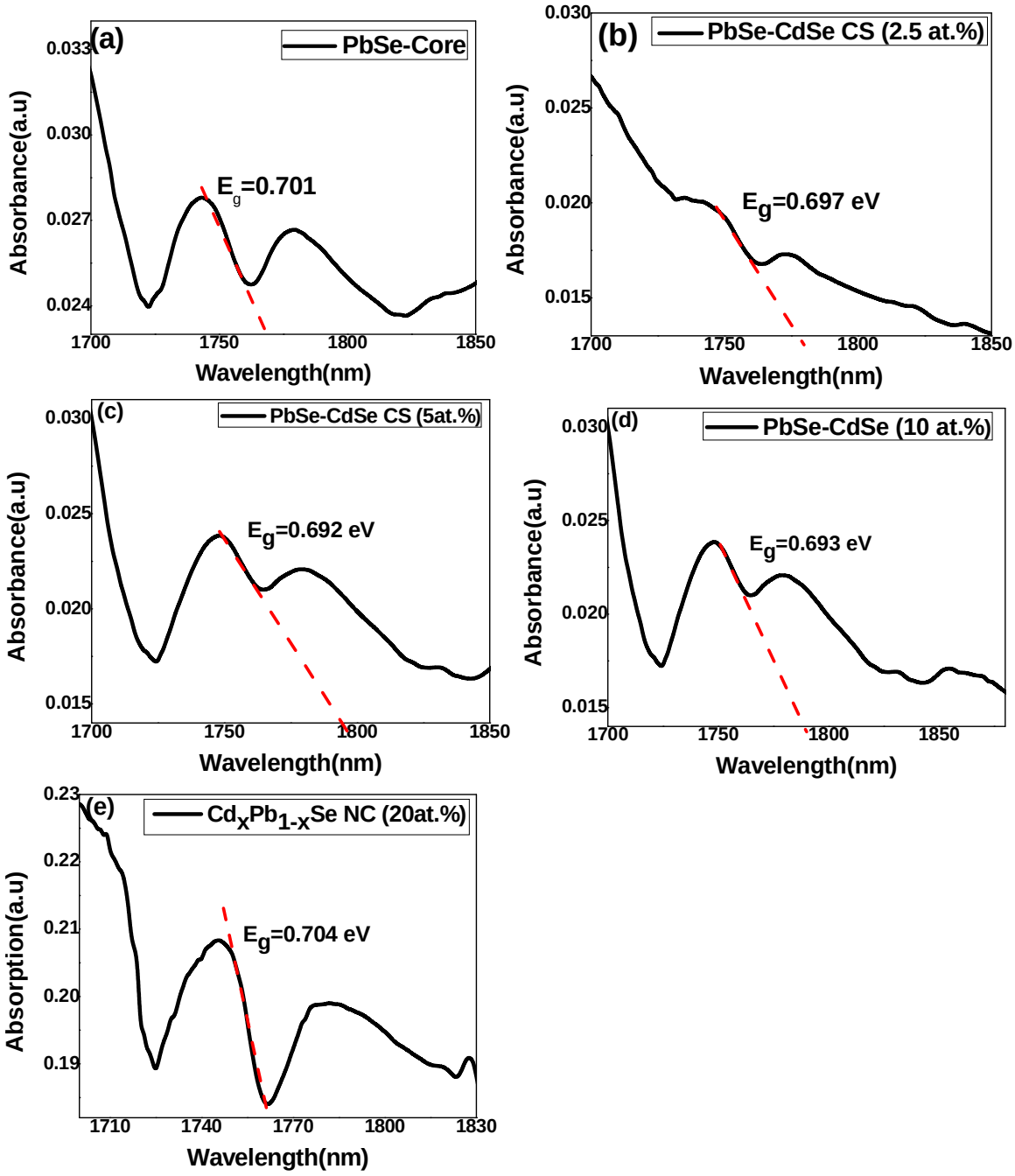

Figure 4.7 Near-infrared absorption spectra of as-prepared (a) PbSe-core(b)PbSe-CdSe core-shell(2.5 at.%),(c) PbSe-CdSe core-shell (5at.%)(d) PbSe-CdSe (10 at.%) & (e) $Cd_XPb_{1-X}Se$ nanocrystallites (NC)(20at.%). immersed in hexane.

Using the Effective Mass Approximation(EMA) the particle size can also be calculated through the absorption curve.

Equation 4.3 shows the relation for effective mass approximation[5]

$$E_R = E_g + \frac{\hbar^2 \pi^2}{2R^2}\left(\frac{1}{m_e^*} + \frac{1}{m_h^*}\right) - \frac{1.786\, e^2}{4\pi \in R} \qquad (4.3)$$

where E_R is the band gap of nanocrystal, E_g is the band gap of the bulk material ,m_e^* and m_h^* is the effective mass of electron and hole of PbSe semiconductor respectively, e is the electronic charge, $\hbar$ is Plank's constant ,ϵ is the dielectric constant inside PbSe-core nanostructure. The calculation of particle size using above relation gives the diameter of the particle nearly 10 nm.

In figure 4.7(b) The visible- IR absorption spectra of PbSe-CdSe core-shell(2.5 at.%), shows absorption edge at λ=1777.67nm.The absorption edge shows red shift with respect to the corresponding spectra of PbSe-core ,which is the signature of core shell formation as the particle size increases with the shell formation. The band gap as calculated using equation 4.2 is 0.697eV and particle diameter calculated using effective mass approximation (given in equation 4.3) is 10.16 nm. In fig.4.7(c) of the above mentioned figure the visible- IR absorption spectra of PbSe-CdSe core-shell (5at.%) shows absorption edge at λ=1794.69nm. The absorption spectra shows red shift with respect to the corresponding absorption spectra of PbSe-core and spectra of PbSe-CdSe core-shell(2.5 at.%) which is the signature of core shell formation as the particle size increases with the shell formation[3] . The band gap in this structure as calculated using equation 4.2 is 0.691 eV. The band gap increases due to the formation of larger size particles as compared to the core structure. The particle diameter as determined using effective the mass approximation relation (given in equation 4.2) is 10.26 nm.

As we move towards increase in concentration of CdO precursor in figure (d) the slight blue shift in the absorption spectra of PbSe-CdSe (10 at.%) with respect to the corresponding spectra for PbSe-CdSe core-shell(5at.%) but still maintains a red shift as compared to the corresponding spectra of PbSe-core. The visible- IR absorption spectra of PbSe-CdSe shows absorption edge at λ=1789.04nm. The band gap in this structure as calculated using equation 4.2 is 0.693eV. In figure 4.7(e) the absorption spectra of $Cd_XPb_{1-X}Se$ (NC) (20at.%). The visible- IR absorption spectra of ternary Pb_xCd_{1-x} Se semiconductor nanostructure shows absorption edge at λ=1760.23nm. The absorption spectra shows blue shift with respect to the corresponding absorption spectra of core PbSe and spectra of PbSe-CdSe core-shell(2.5 at.%), which is the signature of alloy formation. The band gap in this case is 0.704 eV. From the above data we

conclude that the band gap values are higher than the bulk PbSe semiconductor value i.e. 0.28 eV shows the PbSe nanoparticles are quantized.

E_g($Cd_XPb_{1-X}Se$ nanocrystallites(NC)(20at.%). >Eg(PbSe-core) >Eg(PbSe-CdSecore-shell,2.5at.%) >E_g(PbSe-CdSe (10 at.%)) >E_g(PbSe-CdSe core-shell,5at.%).

0.704>0.702>0.697>0.693>0.692

S.No.	system	size (TEM)	Size calculated using EMA
1.	PbSe-core	7 nm	10 nm
2.	PbSe-CdSe core-shell, 2.5at. %	8 nm	10.16 nm
3.	PbSe-CdSe core-shell, 5at. %	10 nm	10.26 nm
4	PbSe-CdSe (10 at. %)	*	*
5.	$Cd_XPb_{1-X}Se$ nanocrystallites (NC) (20at. %).	*	*

Table 4.3.Values of particle size calculated from TEM and EMA. (*TEM & EMA only applicable for spherical particle).

4.4 Optical studies of P3HT: PbSe Nanocomposites

Inorganic PbSe QD's are dispersed in Poly (3-hexyl thiophene) polymer to make PbSe: P3HT nanocomposites .The optical study of nanocomposite includes various phenomenon. Here we focused on study the fluorescence quenching.

Fluorescence quenching refers to any process that decreases the fluorescence intensity of a sample. There are a wide variety of quenching processes that include excited state reactions, molecular rearrangements, ground state complex formation, and energy transfer. Quenching experiments can be used to determine the accessibility of quencher to a fluorophore, monitor

conformational changes, monitor association reactions of the fluorescence of one of the reactants changes upon binding. There are two basic types of quenching: static and dynamic (collisional).

Both types require an interaction between the fluorophore and quencher. In the case of dynamic quenching the quencher must diffuse to the fluorophore during the lifetime of the excited state. Upon contact the fluorophore returns to the ground state without emission of a photon. In the case of static quenching a complex forms between the flurophore and the quencher, and this complex is non-fluorescent. The formatin of this complex does not rely upon population of the excited state. Here we consider the case of collisional quenching.[6]

Collisional quenching occurs when the excited-state fluorophore is deactivated by contact with some other molecule in solution, which is called the quencher. The molecules are not chemically altered in the process.

Fluorescence quenching of P3HT polymer with the addition of PbSe nanocrystal is shown in figure 4.8**.** Fluorescence quenching of P3HT shows that better quenching occurs for higher concentration of PbSe(figure 4.8 (a)} ,in lower concentrations peak intensity shows very minute change, they are almost overlapping curves. As quenching mechanism involves various phenomenon that would takes place during the process, one of the process is charge transfer ,the figure depicts that the charge transfer takes place from P3HT(fluorophore) to the PbSe(quencher).The spectra shows that as we increase the concentration of PbSe, the intensity of P3HT:PbSe nanocomposite decreases due to the fact the electron and hole are generated in P3HT polymer as it is illuminated by the source, when PbSe was added the charge separation occurs. The holes remain in P3HT while electrons move towards PbSe as mobility of electrons is high in PbSe nanoparticles and holes mobility is high in P3HT polymer.

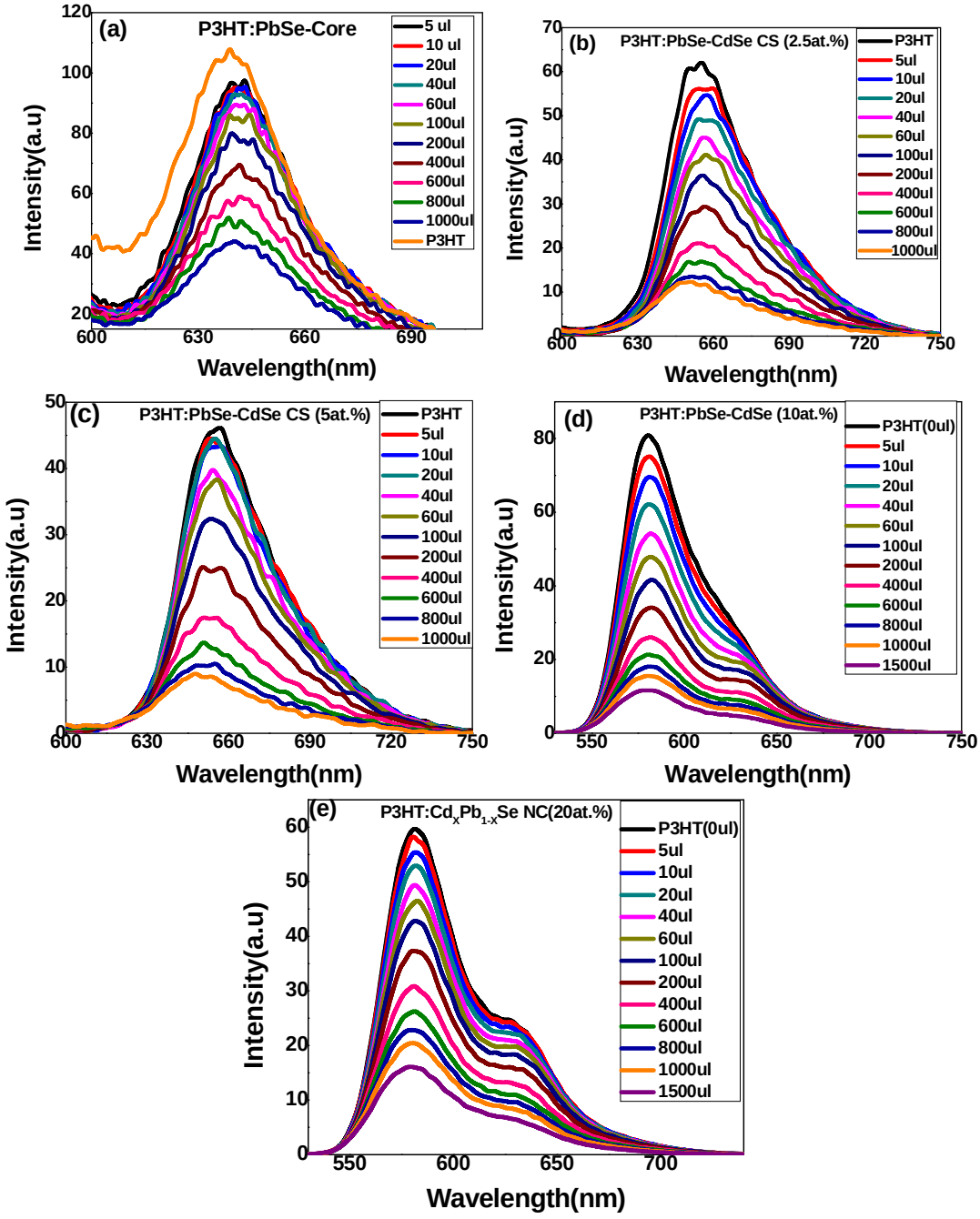

Figure4.8 (a)Fluorescence quenching of P3HT polymer with prepared materials (a)P3HT: PbSe-core (b)P3HT: PbSe-CdSe core-shell(2.5 at.%), .(c) P3HT: PbSe-CdSe core-shell (5at.%).(d) P3HT: PbSe-CdSe (10 at.%).(e) P3HT: $Cd_XPb_{1-X}Se$ nanocrystallites(NC)(20at.%).

In emission spectra of P3HT nanocomposites in figure 4.8 (a-e), the same process of fluorescence quenching takes place only the material which forms nanocomposite was changed. Quenching phenomenon takes place in every curve and it seems to be same in each curve. Only rate of quenching decides the effect of material on the charge transfer mechanism. For collisional quenching, the decrease in intensity is described by the ratio of the fluorescence in the absence of quenching to the presence of quencher by the Stern-Volmer equation:[6,7]

$$\frac{F_0}{F} = 1 + K[Q] = 1 + k_q \tau_0 [Q] \qquad (4.4)$$

where F_0 and F are the observed fluorescence in the absence and presence of quencher, K is the Stern-Volmer quenching constant, k_q is the bimolecular quenching constant, τ_0 is the lifetime in the absence of quencher, and[*Q*] is the quencher concentration. The Stern-Volmer constant is sometimes abbreviated as K_{SV} or even as K_D .

A plot of I_0 / I versus the PbSe concentration [Q] should yield a straight line with its slope equal to K_{sv}. Such plots known as Stern -Volmer plots, are shown in fig.4.9. (a ,b,c,d and e) below for (a)P3HT: PbSe-core,(b)P3HT: PbSe-CdSe core-shell(2.5 at.%), (c)P3HT:, PbSe-CdSe core-shell(5at.%) (d)P3HT: PbSe-CdSe (10at.%).(e) P3HT: $Cd_XPb_{1-X}Se$ nanocrystallites(NC)(20at.%) respectively. The Stern Volmer quenching constant are calculated for all the samples, value for PbSe- core is 240 M-1, PbSe-CdSe core-shell (Cd~2.5at.)% is 830 M-1, PbSe-CdSe core-shell (Cd~5 at. %) is 900 M-1, PbSe-CdSe (Cd~10 at. %)is 710 $M^{-1}$and for. $Cd_XPb_{1-X}Se$ ternary nanocrystallites, (Cd~20at. %) is 340 M^{-1}

The increase in value of Ksv gives the significance of increase in PL Quenching and hence charge transfer in PbSe core-shell structures increases as the shell thickness increases. Even for the Cd~10 at.% and Cd~20at.% the value of Ksv is more than the value for PbSe -core. Increase in value of Ksv gives the evident that interaction between polymer and nanocrystals is increased due to formation of shell over the core sample which removes the surface states as well as satisfies the surface dangling bonds, core-shell nanocrystals are responsible for higher PL quenching due to high charge transfer from polymer to core-shell. In case of Cd~10 at.% the co-existence of core-shell and alloy nanostructures takes quenching constant decrease as compare to the core-shell nanocrystallites, and in $Cd_XPb_{1-X}Se$,(Cd~20at.%) nanostructure the contribution of Cd also effect the rate of quenching. Higher value of quenching constant indicates better charge transfer between polymer and PbSe coreshell structures.

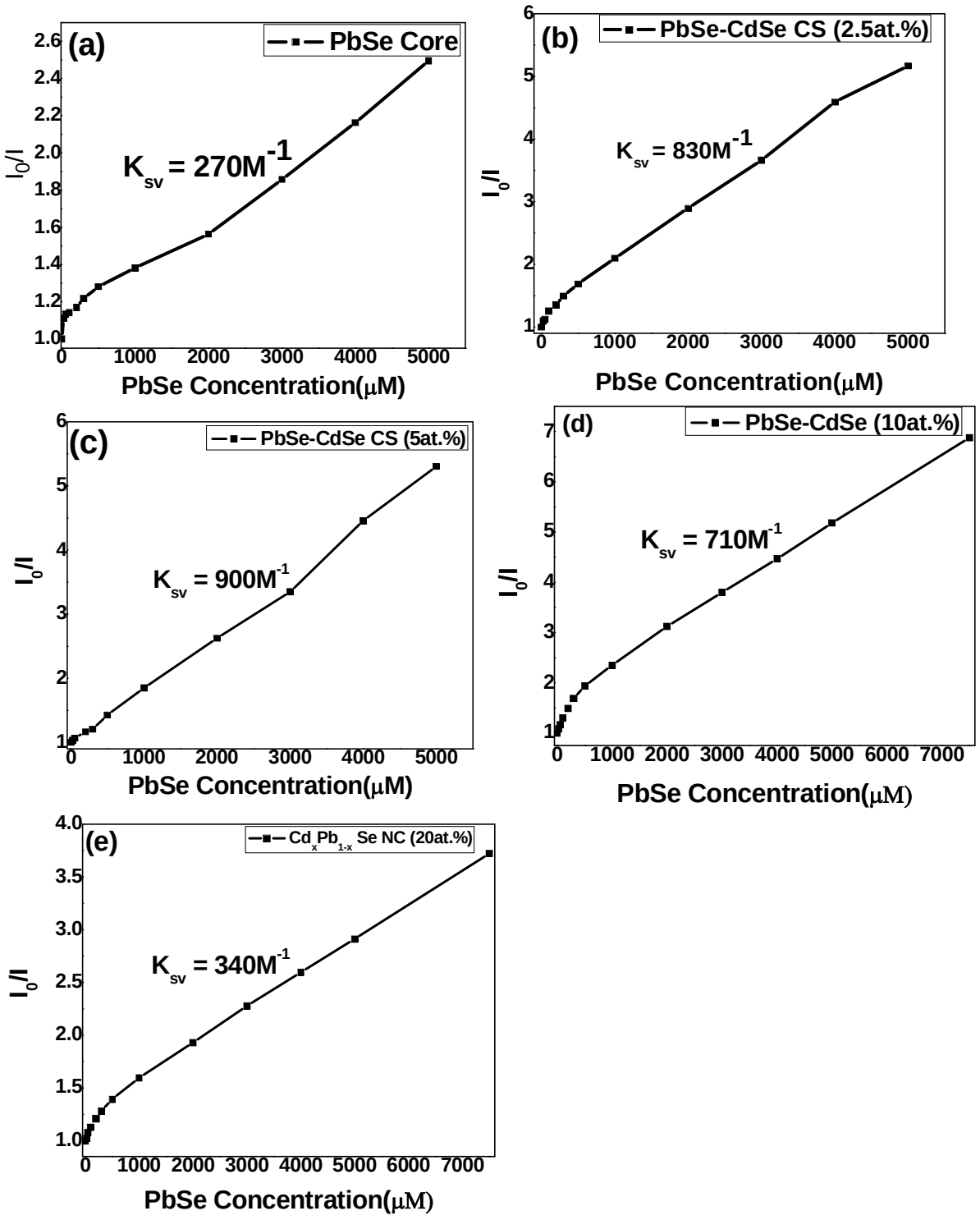

Figure4.9 (a)Stern-Volmer plots of (a)P3HT: PbSe-core (b)P3HT: PbSe-CdSe core-shell(2.5 at.%), .(c) P3HT: PbSe-CdSe core-shell (5at.%).(d) P3HT: PbSe-CdSe (10 at.%).(e) P3HT: $Cd_XPb_{1-X}Se$ nanocrystallites(NC)(20at.%).

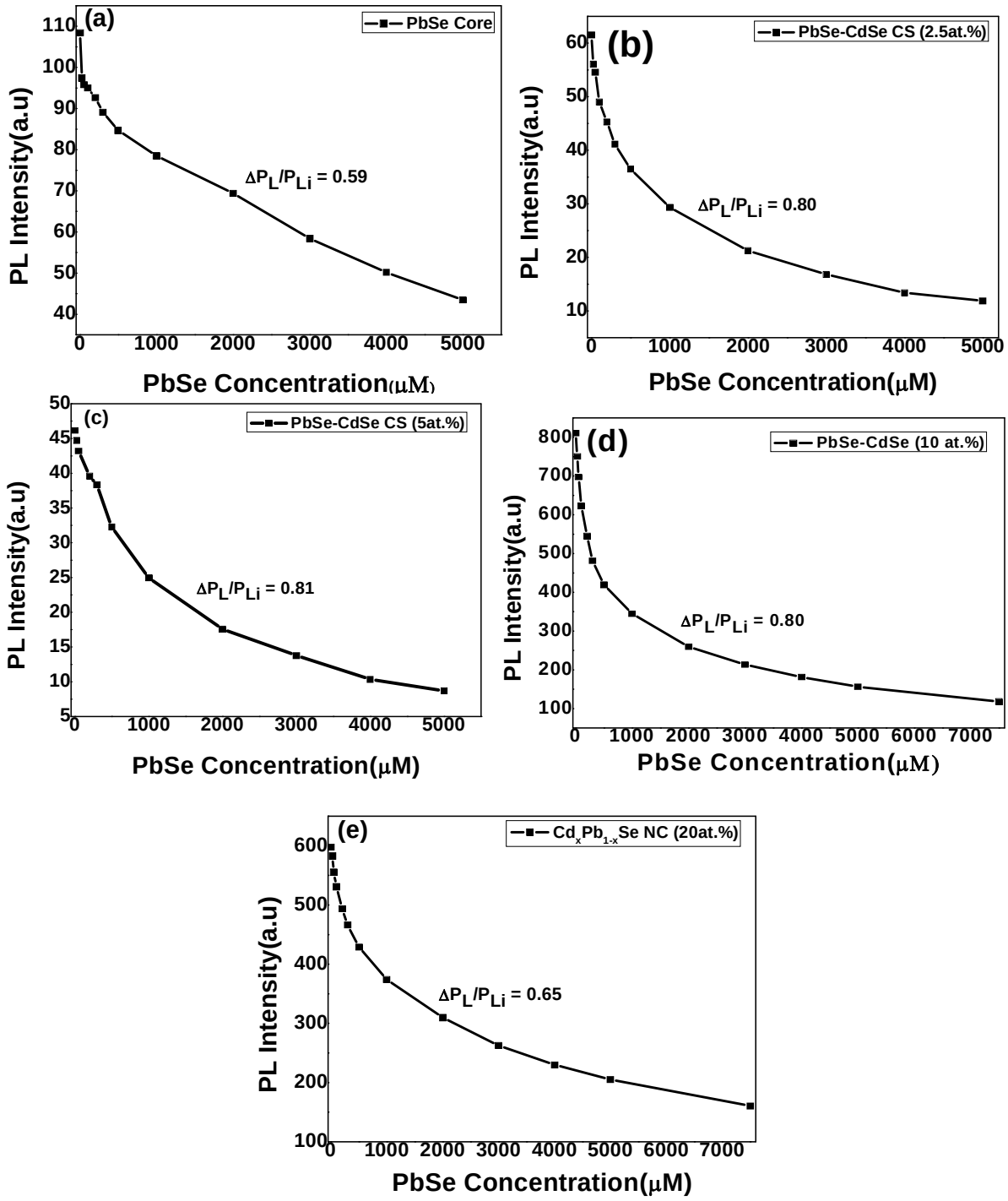

Figure4.10 Emission intensity profile of P3HT: PbSe nanocomposites as a function of PbSe concentration for all (a)PbSe- core and (b)&(c)PbSe-CdSe core-shell structures respectively.(c) &(d) PbSe-CdSe & Cd_X $Pb_{1-X}Se$ nanocrystallites.

Fig.4.10 (a),(b)(c),(d) and(e) shows the emission intensity profile of P3HT: PbSe nanocomposites as a function of PbSe concentration for all PbSe QDs and core shell structures respectively. As evident from the fig.4.6 (a and b,c), that rate of PL decays ΔPL/PLi for P3HT: PbSe-CdSe core-shell Cd~2.5at.%.and Cd~5at.%.are 0.80 and 0.81 respectively, are better as compared to P3HT: PbSe-core for which ΔPL/PLi is 0.59. In case of PbSe-CdSe nanostructure having Cd~10 at.% ,shows higher value of ΔPL/PLi i.e 0.80 than core sample as well as $Cd_X Pb_{1-X}Se$ nanocrystallites also show better result having value 0.65.

PL Intensity decay of P3HT polymer with PbSe-CdSe core-shell nanostructures is maximum, which shows better charge transfer. It is due to efficient removal of surface trap states due to the formation of shell on PbSe-core surface as compared with PbSe-core, it facilitates efficient charge transfer between donor and acceptor leading to the separation of photo excited bound electron-hole pairs in the polymer and hence efficient quenching of PL emission intensity.

References

1.C B Murray, S. Syun, W. Gaschler, H. Doyle, T.A. Betley, C R Kagan,

IBM J. Res. Dev. 45 (2001) 47.

2*. Umesh Kumar, Shailesh N Sharma, Sukhvir Singh, M. Kar, V.N . Singh, B. R. Mehta, Rita Kakra, Material Chemistry and Physics 113(2009) 107-114.

2.Karuppasamy kandasamya, harkesh b singha J. Chem. Sci., Vol. 121, No. 3, May 2009, pp. 293–296.

3.Jeffrey M. Pietryga,Donald J. Werder, J. AM. CHEM. SOC. 9 VOL. 130, NO. 14, 2008.

4.Jiasheng Xu, Jie Zhang, Jianhua Qian Materials Letters 64 (2010) 771–774.

5. A. Meijerink, A. J. Houtepen, et al.small 2008, 4, No.1, 127–133.

6. Spring 2005, Handout Number 8 Page 3 of 11, Techniques in Biophysics 250.690 Karen Fleming, pdf report.

7. Kusum Kumari, Umesh Kumar, Shailesh N Sharma, J. Phys. D: Appl. Phys. 41 (2008) 235409 (9pp).

CONCLUSION:

- Single pot synthesis of PbSe-CdSe nanocrystallites has been done for the very first time unlike to other approaches (like SILAR's process & Partial Cation Exchange Method) where double pot synthesis was used.

- By mere variation of CdO, we get three regimes PbSe-core, PbSe-CdSe core-shell $Cd_XPb_{1-X}Se$ nanocrystallites, we get composition tunable nanocrystallites.

- This method also prevents the oxidation of core sample before as that might be happened in two pot synthesis. Since the nucleation of PbSe largely depends on the reaction temperature, lowering the temperature can completely stop the nucleation process, and thus control the particle size distribution very easily. The particles were found to be in nanometer range and the optical absorption investigations showed them to be in quantum confined states.

- PbSe–CdSe core-shell nanocrystals shows higher fluorescence quenching indicating efficient charge transfer as compare to PbSe-core &ternary nanocrystallites.

- These PbSe-CdSe composition tunable nanostructures can be effectively used for OPV because of effective charge transfer of electrons and holes.